

Spatio–Angular Microscopy

PhD Thesis

Martin Kielhorn

July 2012

Abstract

Photobleaching and phototoxicity pose a problem in live cell imaging. Fluorescence imaging induces reactive oxygen species in observed organisms which can alter the behaviour of the sample. Hence, minimising the light exposure is an important goal.

We augment a wide field epifluorescence microscope with two spatial light modulators. By controlling the spatial excitation pattern and the angle of illumination, we can adapt the illumination to the specimen. In many cases, this technique will create exposures with reduced excitation of the out-of-focus fluorophores, resulting in better image quality and less phototoxicity.

Our custom software is used to obtain an initial image stack of the specimen. Subsequent image sections are exposed with excitation patterns that account for the previous image stack. Depending upon the distribution of fluorophores, this adaptive exposure can considerably reduce photobleaching and phototoxicity.

Preface

Matthae, Manfred and Schreiber, Lothar and Faulstich, Andreas and Kleinschmidt (2003)

The work described in this thesis was carried out between June 2008 and March 2013.

In chapter 1, we introduce photophysics of fluorescence and emphasize the importance of oxygen for phototoxicity. Furthermore, we also explain conventional microscopes and CCD cameras.

In chapter ??, we compare some state-of-the-art techniques for illumination control in microscopes. Particularly in section ??, we discuss the micro-lens based light field microscope by Levoy's computational photography group, which imaged the toy soldier in 2003.

In chapter ??, we describe our microscope and in chapter ??, we show some images, taken with illumination control in our prototype.

There is also an extensive appendix where we document more technical issues like read noise calibration of a camera (Appendix ??) or finding a rigid transform between a camera and a display (Appendix ??).

In the appendix, we also describe a completely different approach for spatio-angular illumination based on holography (Appendix ??) and we document an interferometric attempt to convert our precise programmable phase mask into a spatial intensity modulator (Appendix ??).

Note that the Appendix ?? describes a modification of our prototype with a spatial light modulator that receives data from a graphics card. A higher bandwidth makes this approach more useful than the prototype described in the main text and we tried to implement this first. However eventually, it proved too difficult to trigger the components in this configuration and we switched to the more predictable USB-controlled display as described in the main body of the text.

The appendix also contains some theoretical explanations of raytracing (Appendix ??), computational optical sectioning (Appendix ??) and the wave-optics based simulation of our microscope (Appendix ??).

Source Code Availability

Source code that has been developed during this project is available on <https://github.com/plops/mma>. It contains implementations for:

- illumination planning based on raytraces (see Appendix ??)
- moving the z–stage of a Zeiss Axiovert 200M microscope body
- controlling an Andor Clara camera using the Andor SDK version 2. For the other cameras following below, control software was written:
 - Photometrics Cascade II (interface to unsupported closed-source driver, only works on very old 32-bit Linux kernels)
 - mvBlueFox 102G using the SDK
 - Logitech Pro 9000 using a generic Video4Linux interface
 - Andor sCMOS using Andor SDK version 3
- displaying patterns using a graphics card that supports OpenGL on a ForthDD SXGA ferroelectric LCoS display
- controlling a stand-alone ForthDD WXGA 3DM display controller using USB
- estimating the parameters of a rigid transformation between camera and LCoS display (see Appendix ??),
- controlling the micro-mirror array by Fraunhofer IPMS using their SDK
- some specific image processing tools:
 - three-dimensional convolution and Fourier transforms
 - drawing of lines and ellipsoids in volumes
 - rasterization of triangles (for creating shadow maps in the BFP, see section ??)
 - calculation of optical transfer function for high NA objectives
 - localization of spherical nuclei in volumetric data (parts of the algorithm as described in Santella et al. (2010))

The main development was done using GNU Linux. However, portability was kept in mind and most of the code was made to work with Microsoft Windows as well.

Acknowledgements

It is my pleasure to thank all those who have made this thesis possible. First and foremost, I owe my deepest gratitude to my supervisor Rainer Heintzmann for giving me the opportunity to become part of his research group at King's College London and later in the Institute of Photonic Technology in Jena.

I owe my sincere thanks to Kai Wicker, Jakub Nedbal, Susan Cox, Daniel Appelt, Ondřej Mandula, Ronny Förster, Ivana Šumanovac, Eckhard Birkner, Kathrin Klehs and all the other members of our group for valuable discussions, support and review of the manuscript.

My sincere thanks to the European Union Framework Programme 7 (project number 2115597) for the studentship on this project. I also thank Erhard Ipp, Günter Zöchling, Vincent Galy, QueeLim Ch'ng, Jörg Heber, Mark Eckert, Dirk Berndt, Joel Seligson, Jean-Yves Tinevez and Florian Rückert for helpful collaboration.

Furthermore I highly appreciate the input of Herbert Gross, Miroslav Grajcar, Edward Rosten, Christophe Rhodes, Paul Khuong, Nikodemus Siivola, Gabor Melis and Luís Oliveira. Occasionally, the expertise and insight of them steered me into right direction or greatly simplified problems I faced.

Finally, I wish to thank the authors and contributors to the following software projects: Linux, GCC, Emacs, SBCL (Rhodes 2008), Maxima, Micromanager (Edelstein et al. 2010), DIPimage, Wireshark, Latex, Inkscape, Gimp, ImageJ/Fiji (Abràmoff et al. 2004; Schindelin et al. 2012) and Blender. These free software projects and their communities are invaluable to my work and greatly enhance my efficiency.

The work presented in this thesis is my own, unless I cite a reference.

M. K.

Jena, Germany

March 2013

Contents

1. Introduction	10
1.1. Phototoxicity in life sciences and the model organism <i>C. elegans</i> .	11
1.2. Photophysical principles of phototoxicity	15
1.3. Conventional microscopes	18
1.3.1. Ray-optical description of a large-aperture lens	18
1.3.2. Wave-optical theory for image formation in a fluorescence microscope	19
1.3.3. Illumination in a wide-field epifluorescence microscope	25
1.3.4. Phototoxicity in conventional microscopes	27
1.3.5. Conclusion	27
1.4. Image detectors in wide-field microscopy	27
1.4.1. Introduction	27
1.4.2. Photon shot noise and read noise	28
1.4.3. Comparison chart for detector selection	31
1.4.4. Calibration of the EM-CCD gain	34
1.4.5. Conclusion	35
2. Methods of controlling illumination patterns	37
2.0.6. 2-photon laser scanning fluorescence microscopy	37
2.1. programmable array	37
3. The concept of spatio-angular microscopy	38
3.1. Motivation	38
3.2. An imaging protocol with spatio-angular illumination control	42
3.2.1. Description of an exemplary biological specimen	42
3.2.2. Preparation of living embryo samples	42
3.2.3. Sectioning through structured illumination	43
3.2.4. Computer model for the integration of a priori knowledge about the biological events	43
3.2.5. Illumination optimization by means of raytracing	45

Contents

4.	Description of our prototype for spatio-angular illumination	47
4.1.	Description of the optical components	47
4.1.1.	Ensuring homogeneous illumination	49
4.1.2.	Fourier optical filter for contrast generation on pupil plane SLM	51
4.1.3.	Relay optics between pupil plane and focal plane SLM . . .	54
4.1.4.	Contrast generation on focal plane SLM using polarization	55
4.1.5.	Variable telescope as tube lens	55
4.2.	Electronic control of the component	56
5.	Experimental results with spatio-angular microscope	58
6.	Discussion	63
6.1.	Outlook	67
A.	EM-CCD camera calibration	68
A.1.	Andor Basic code listing for automatic image acquisition	68
A.2.	Python code listing for the read noise evaluation	71
B.	Optical sectioning by structured illumination	74

Nomenclature

- β Transversal magnification of an objective $\beta = f_{\text{TL}}/f$, for Zeiss lenses the magnification β is written on the objective and the focal length of the tube lens is defined as $f_{\text{TL}} = 164.5 \text{ mm}$, page 18
- \mathcal{E} Etendue, information capacity, light gathering capacity or space-bandwidth product; its value is related to the number of point spread functions that can be resolved in the field., page 26
- Ω Excitation dose in $\text{J}/(\text{cm}^2 \text{stack})$, page 14
- Φ_e Radiant flux of excitation light in watts, page 14
- $\mathbf{r} = (r_x, r_y, r_z)^T$ Three-dimensional spatial coordinate, page 21
- $\mathbf{r}_t = (r_x, r_y)^T$ Transversal two-dimensional spatial coordinate, page 21
- $\mathbf{v} = (v_x, v_y, v_z)^T$ Three-dimensional spatial frequency, page 21
- $\mathbf{v}_t = (v_x, v_y)^T$ Transversal two-dimensional spatial frequency, page 21
- $\tilde{u}(\mathbf{v})$ Fourier transform of scalar field as a function of spatial frequencies, page 21
- $u(\mathbf{r})$ Scalar field as a function of spatial coordinates, page 21
- chief ray Ray from the periphery of the field through the center of the entrance aperture, page 18
- EM-CCD Electron multiplying charge-coupled devices, page 10
- entrance aperture Projection of the limiting aperture of the optical system into object space, page 18
- Ewald sphere Transfer function of free space, page 21
- I²M Image interference microscopy (Gustafsson et al. 1999),, page 25
- LED light emitting diode, page 49

Contents

marginal ray Axial ray through the periphery of the entrance aperture, page 18
USB Universal Serial Bus., page 64

1. Introduction

my device	<p><code><sec:intro></code></p> <p>In this work I discuss a modification of a fluorescence microscope that minimizes the toxic effects of the excitation light.</p>
phototoxicity	<p>In the following introductory chapter I describe what phototoxicity is and how it comes about. Then I give an example of how it influences biological observations in a developing <i>C. elegans</i> embryo and describe how this particular biological system can be used to evaluate and compare the phototoxicity of different microscopes.</p>
cameras	<p>Later in this chapter I give an overview of image formation in the wide-field microscope and I describe its principle limitations regarding resolution and depth discrimination. Furthermore I discuss the two most important current image detector technologies — electron multiplying charge-coupled devices (EMCCD) and scientific complementary metal–oxide–semiconductor (sCMOS).</p>
labelling, switching	<p>Regardless of whether it is the picture of earth captured by an orbiting satellite, the x-ray motion picture of a running dog or the time-lapse recording of a blooming flower. Images capture our imagination and they are a good starting point to develop new models and theories.</p> <p>This is particularly true for microscopy. Only after people became aware of microorganisms by direct observation, medieval quack could finally be overcome and modern medicine based on the scientific method flourished instead.</p> <p>Even today — with electron microscopes, magnetic resonance tomography and sequencing machines — optical microscopy still is an indispensable tool for research of living organisms.</p> <p>Fluorescence microscopy is of particular importance: It enables the scientist to selectively label a particular type of molecule in living cells and observe how they perform their biological function.</p> <p>Besides localizing molecules it is possible to measure physical quantities inside of the sample. There are, for example, fluorescent labels that report membrane potentials or viscosity inside of cells.</p> <p>Finally, it is even possible to exert a controlling function with the excitation light: There are compounds that locally release chemicals when illuminated and</p>

1. Introduction

there are genetically encoded ion channels that can be switched by light (?).

However, the excitation light introduces unnatural and potentially deleterious energy into the specimen. If the exogenous light harms the observed organism in any way, this effect is called phototoxicity.

There are a number of techniques that can reduce phototoxicity: Two photon excitation, controlled light exposure, selective plane illumination, highly inclined and laminated optical sheet, and oblique plane microscopy. I introduce them in chapter 2. These techniques have different pros and cons and not all are equally suited for a specific problem, e.g. selective plane illumination is very effective, but it needs two perpendicular lenses and can not be used for multiwell plates or to observe the liver of a living, adult mouse.

In this work I present an approach that makes use of modern display and camera technology. We only modify the microscope's illumination path, the space around objective lens and specimen remains as accessible as in any conventional wide-field microscope.

1.1. Phototoxicity in life sciences and the model organism

C. elegans

:intro-phototoxicity) The partner in our project who is responsible for decisions related to life sciences and biology is Institut Pasteur (Paris, FR). They work on infectious diseases.

In order to motivate the importance of phototoxicity, I would like to portray an elegant drug screening experiment which I have seen on one of my visits in Paris: An automatic microscope continuously images a cell culture in multiwell plates. These cells carry a pathogen. The pathogen, the nuclei of the cultured cells and the membranes of the cells are each stained with a different fluorophore. The cells in each well of the plates are exposed to a different chemical.

A chemical is considered a hit and will be investigated during further trials, when the time lapse images show that the culture cells stay healthy and the number of pathogens decrease. As neither people nor animals come to harm, this screening experiment is an impeccable method to systematically understand and hopefully heal certain diseases. However, this experiment does not work very well, if the excitation light — and not the drug — kills the pathogens. The effect of phototoxicity should therefore be minimized.

Now one would hardly develop a microscope and directly test it with dangerous pathogens. As part of our collaboration, the Institut Pasteur therefore developed

1. Introduction

a safe biological test system that is relatively easy to maintain (?) and allows to test the phototoxicity of various microscopes (?).

The basis of the system is the embryo of the organism *C. elegans*. These are small invertebrates. The adult form is approximately 1 mm long. Their anatomy and development are comparatively simple and have been well characterized (??).

We use embryos of a genetically modified strain¹ that expresses eGFP tagged histones (enhanced green fluorescent protein, excitation maximum 488 nm, emission maximum 509 nm). Histones are incorporated into the chromatin during cell divisions, i.e. the nuclei of our worms fluoresce green. The mother worm passes a sufficient amount of these proteins into the cytoplasm of the embryo. In the beginning of its development the embryo entirely relies on this reserve of histones. Only in a much later stage — certainly not during the first few hours, that we observe — it will form its own histones.

embryo example

Figure 1.1 compares time-lapse experiments on three different *C. elegans* embryos with varying excitation intensities.

reproducible development

The lineage tree of two developing *C. elegans* embryos is the same. With all other factors being equal, particularly if the temperature is constant at $21 \pm 1^\circ\text{C}$, two different embryos will develop at the same speed from egg to fertile adult in three and a half days.

At the beginning of the experiment, embryos are removed from their mothers at an identical stage, before any cellular divisions have occurred. Then a z-stack of the egg with 41 slices and one micron z-sampling is obtained every two minutes.

The columns in Figure 1.1 depict three different embryos whose development was imaged according to this protocol for two hours and 38 minutes with different excitation powers.

The figure displays the maximum intensity projections of the z-stacks. In order to make the cell nuclei visible in all images, I normalized the data to the same range. As can be guessed from the photon shot noise, the upper left image contains the least number of fluorescence photons, and the upper right the most.

An analysis of the time-lapse data show that one hour into the experiment the embryo with the highest excitation dose (right) has stopped developing and its fluorophores are strongly bleached. Some cells even turned apoptotic and went into programmed cell death.

After two hours and 38 minutes the experiment was stopped and the embryo which was exposed to the lowest dose (left) has developed the largest number of cells. The middle embryo ceased developing while the right embryo died even

¹Our strain has WormBase ID AZ212 (?).

1. Introduction

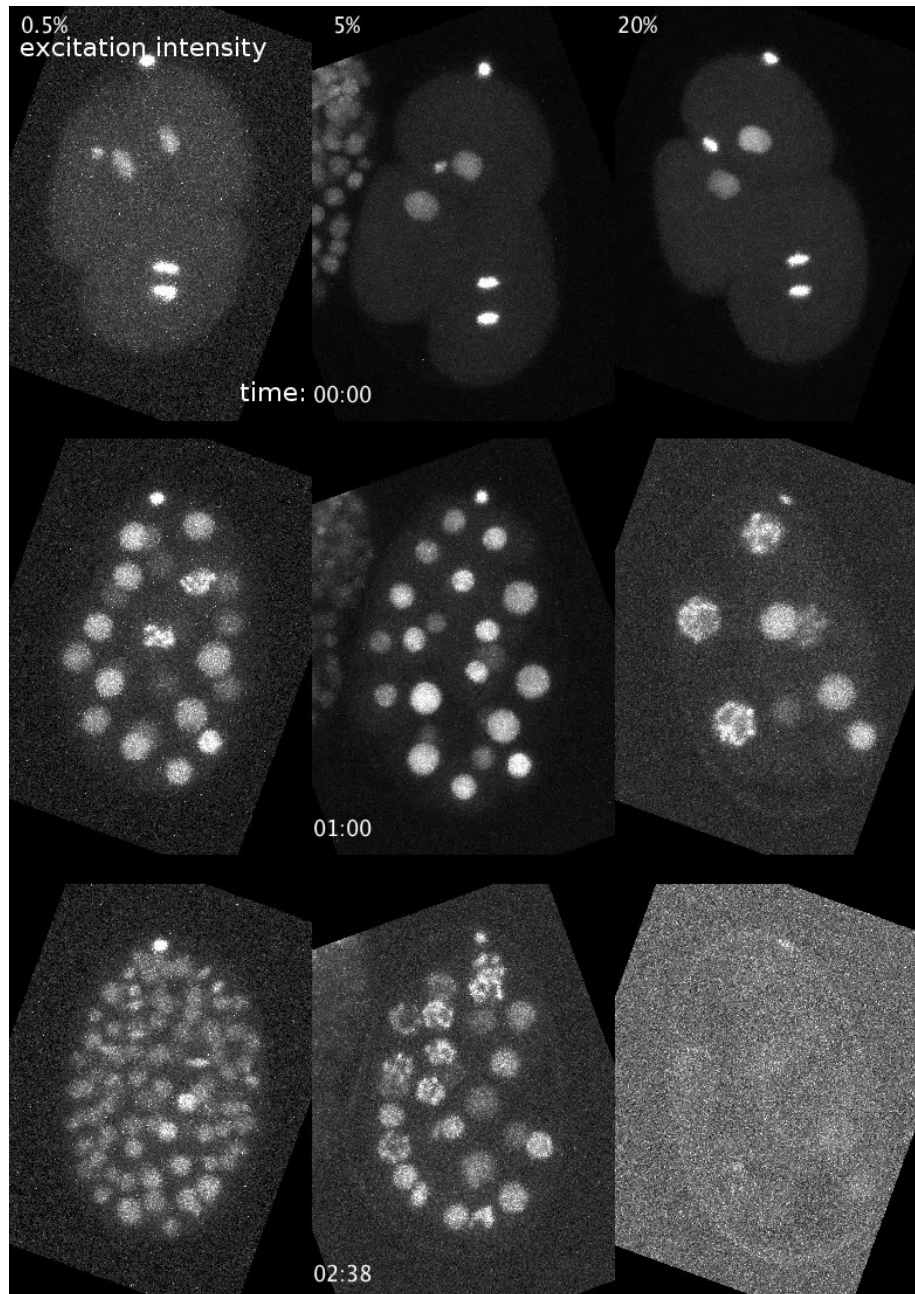


Figure 1.1.: Phototoxic effects while imaging the embryonal development of three *C. elegans* embryos (strain AZ212, histone-2B tagged with eGFP) with different excitation intensities. The embryo with lowest excitation dosage (left) develops fastest. The embryo with the highest dosage (right) ceases development and nearly all fluorophores are bleached after the experiment. Images by J.-Y. Tinevez (Institut Pasteur, Paris, FR).

{fig:celegans-devel}

earlier and nearly all its fluorophores are bleached at the end of the experiment. In Figure 1.2 I reproduce quantitative data from ?. Each data point in this

1. Introduction

graph corresponds to a two hour time-lapse imaging experiment of a *C. elegans* embryo in a wide-field microscope. From a very low excitation up to a certain threshold dose the development is not affected by the light and approximately 50 cells develop during the two hours.

For a dose above the threshold the development is slowed due to phototoxicity and the number of cells at the end of the experiment decreases.

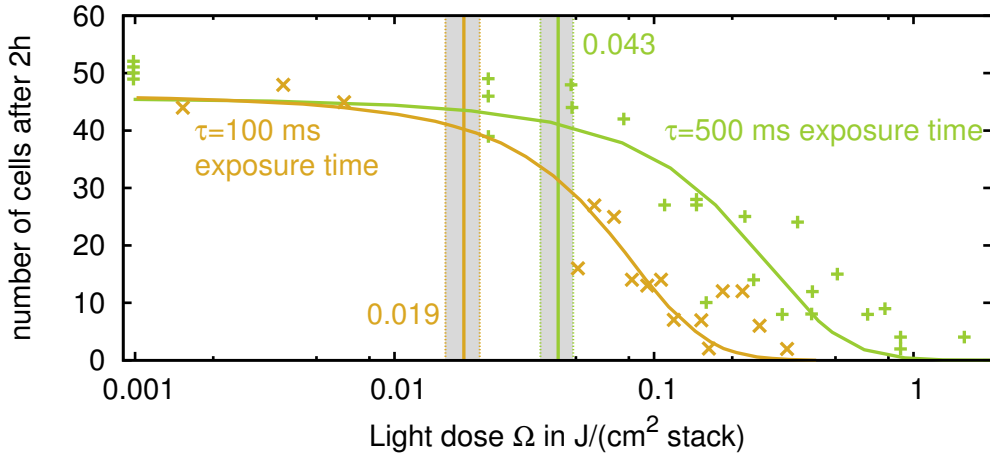


Figure 1.2.: Longer exposure times are less phototoxic. Each data point corresponds to one embryo that developed under a particular excitation dose for two hours. The solid lines are sigmoidal fits to the data. Also indicated are the two phototoxicity thresholds given by the inflection point of the sigmoid and their 95% confidence intervals. This data was provided by J.-Y. Tinevez (Institut Pasteur, Paris, FR) and is also published in ?.

The orange data points in the diagram correspond to a per slice integration time τ of 100 ms and for the green data the integration time is five times higher.

The dose Ω on the x -axis is calculated as

$$\Omega = \frac{\Phi_e n \tau}{A}, \quad (1.1)$$

with integration time τ , area A of the illuminated field, the number of slices $n = 41$ and radiant flux Φ_e of the excitation light, as measured in the pupil.

Naively one would assume that it should not make any difference if the excitation light dose is administered with 100 ms or 500 ms exposures but these data show that a longer exposure time and low intensity are less phototoxic.

These results agree with an earlier study in tobacco plants (?). They investigate cell death a few days after illumination and find that there is a threshold dose

1. Introduction

below which no phototoxicity can be detected, and that this threshold decreases with light intensity. Dixit and Cyr show that the damage is caused by reactive oxygen species and they explain the shift of the phototoxicity threshold by the limited capacity of the cells' scavenging system for those radicals. They also predict the existence of redox-sensitive checkpoints in the mitotic division cycle.

In summary this section describes how to measure phototoxicity with biological specimen. The next section gives an overview of the underlying photophysics and the rest of this work describes our attempt to build a microscope with reduced phototoxic footprint.

1.2. Photophysical principles of phototoxicity

`<sec:photophysics>`

Here I give a short overview of fluorescence of molecules in order to introduce the terms photobleaching and phototoxicity.

energy levels

A fluorophore is a molecule that can absorb and subsequently emit light. During the absorption of a photon the molecular orbital transitions from the electronic ground state S_0 to an excited state S_1 . The lifetime of the excited state S_1 is in the order of a few nanoseconds. A Jablonski diagram, as depicted in Figure 1.3, summarizes information about the energy levels of a molecule and possible transition processes.

The majority of known stable and bright fluorophores absorb and emit in the wavelength range between 300 nm and 700 nm. Photons at the high energy end of this range can excite molecules into higher energy levels S_n , ($n > 1$) than the first excited state; these states are unstable and hardly return to the ground state S_0 . On the other side of the spectrum: a molecule that absorbs in the near-infrared (> 700 nm) has a low-lying excited singlet state S_1 and therefore potentially increased reactivity and a high probability for a non-radiative transfer back into the ground state S_0 (?).

The term *Stokes' shift* describes the frequency shift between the absorbed and emitted photon; the energy difference is lost as heat to the fluorophore molecule and surrounding solvent. For the practical implementation of fluorescence microscopes this is significant, as it enables to separate excitation and emission light with a dichroic beam splitter.

The excitation probability of a fluorescence molecule depends on the orientation of its dipole axis relative to the plane of vibration of the excitation field. Especially if the molecule is not rigidly bound to a bigger structure or embedded in a viscous

1. Introduction

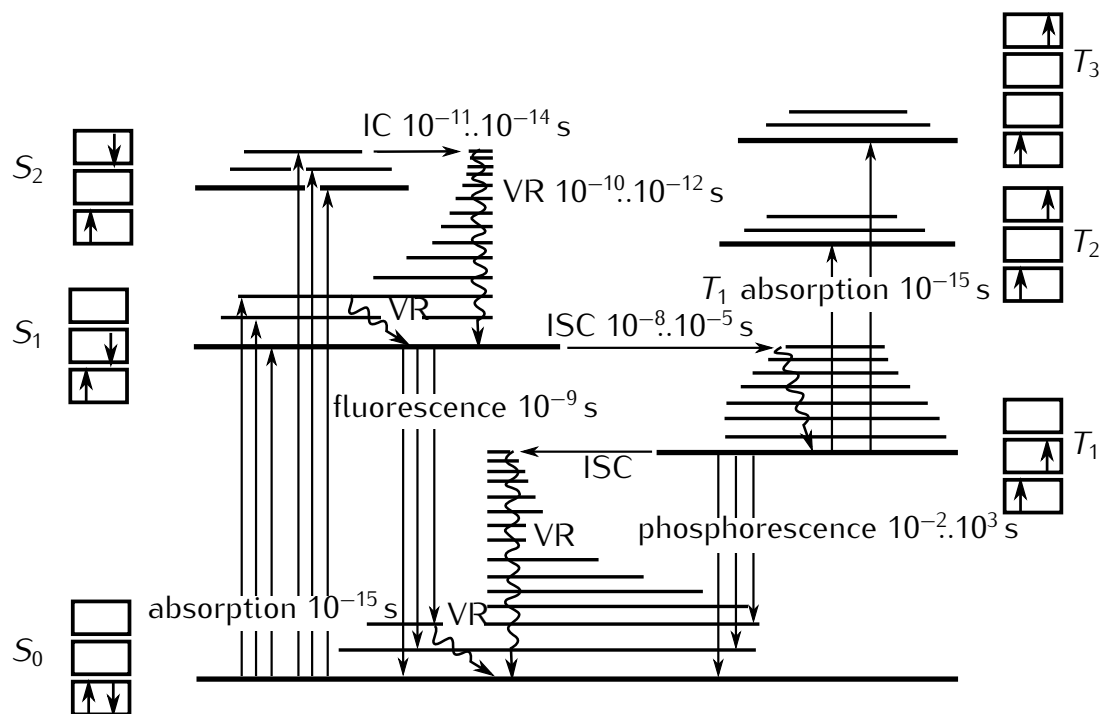


Figure 1.3.: The Jablonski energy level diagram of an illustrative fluorescent molecule. The boxes depict orbitals, up and down arrows symbolize the spin of the outer electrons. Fat horizontal lines represent electronic states. Thinner lines indicate vibro-rotational states. Various processes are shown with their typical time scales. VR = vibro-rotational relaxation, ISC = intersystem crossing, IC = internal conversion (inspired from ?).

(fig:flu-level)

solvent it will reorient its dipole during the fluorescence lifetime and emit the fluorescence photon in a random direction. We use this in the next section to describe image formation in the fluorescence microscope.

The triplet states T_n play an important role in photobleaching. Pure electronic absorption of one photon has no effect on the spin of an electron and therefore the transition from singlet states S_n into the triplet state T_n should not occur. However, interaction with the nuclei can mediate this spin transition. Therefore, in fluorophores this transition has a small probability, resulting in long lifetimes of the triplet state T_1 .

? show that excitation of higher triplet states T_n is the predominant reactive process for photobleaching in vacuum. In particular they measured that one rhodamine 6G molecule *in vacuum* can emit more than 1×10^9 photons before it bleaches, if the excitation intensity is low enough ($\sim 1 \text{ W/cm}^2$) to prevent decay over triplet states.

1. Introduction

In normal atmosphere the prolonged lifetime of the triplet state T_1 makes it highly likely for the fluorophore to react with molecular oxygen O_2 . Oxygen is abundant and has a triplet ground state $^3\Sigma$ with two unpaired electrons of parallel spin in its π^* -orbitals (see Figure 1.4).

(?)

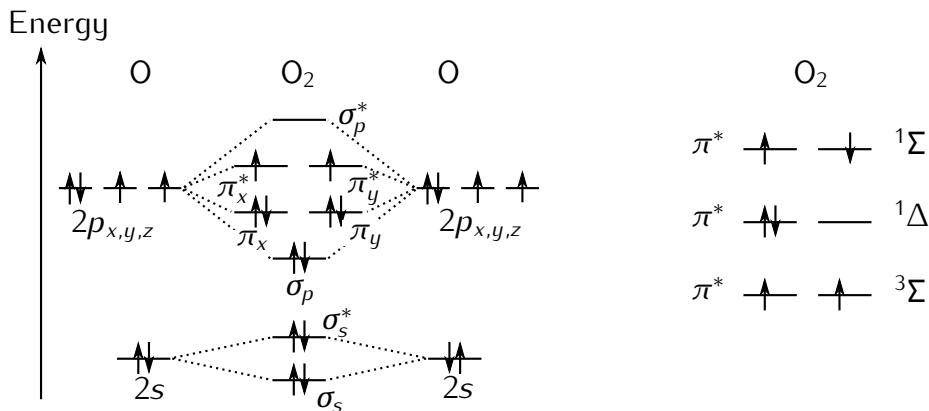


Figure 1.4.: **left:** Schematic that depicts how the orbitals of the oxygen molecule are formed from the atomic orbitals. **right:** Molecular oxygen has the lowest energy in its triplet state $^3\Sigma$ where the spins of the two outer π^* -electrons are parallel. Inspired from ?.

(fig:oxygen)

If a ground-state oxygen molecule comes into physical contact with a T_1 fluorophore, the energy of the latter can be transferred by an electron exchange energy transfer mechanism in which the orbitals directly interact with each other (?, p. 438 and ?).

During this reaction, which is also known as triplet-triplet annihilation, two forms of singlet oxygen form in competition: The lower energy state $^1\Delta$ and the short-lived, higher energy state $^1\Sigma$ that immediately ($T_{1/2} \sim 10^{-9}$ s) sends out a 1268 nm photon and decays into $^1\Delta$.

The resulting singlet oxygen $^1\Delta$ is very reactive. In a typical specimen it diffuses only a few tens of nanometres until it reacts with another molecule.

(FIXME 2000 greenbaum measures oxygen production, bernas 2004 anoxia gfp)

Nowadays many methods are known to reduce photobleaching: Substitute oxygen with noble gases or remove it enzymatically (?, p. 89), depopulate the triplet state by adding reducing as well as oxidizing agents to the solvent (?) or couple a triplet quencher directly to the fluorophore (?, p. 19). For fixed samples it helps to change the solvent or polymer.

In living specimen these techniques may reduce photobleaching, but they can also have a detrimental effect on the biological system itself. Removing oxygen

1. Introduction

will quite certainly have a negative effect. In order to reduce phototoxicity it makes sense to think about the light management in the microscope.

1.3. Conventional microscopes

The wide-field fluorescence microscope does not excite fluorophores of the specimen in an optimal way. In this section I outline how these microscopes work and explain how out-of-focus blur severely limits their performance. I introduce the terms point spread function, optical transfer function and etendue.

1.3.1. Ray-optical description of a large-aperture lens

A microscope, is a device that collects light coming from one plane and forms a magnified image on a camera. Figure 1.5 b) shows a schematic representation of the detection path of a wide-field microscope.

The main components are an objective lens with focal length f and a tube lens TL1 with focal length $f_{TL} > f$. Sample, lenses and camera are arranged in double-telecentric configuration, i.e. the sample is located in the front focal plane of the objective, the tube lens is at distance f_{TL} behind the pupil (i.e. the back focal plane of the objective) and the camera is in the focal plane behind the tube lens.

Light from the sample is collimated by the objective lens and re-imaged by the tube lens. The lateral magnification β is given by the ratio of the focal lengths of the two lenses:

$$\beta = \frac{\overline{O'P'}}{\overline{OP}} = \frac{f_{TL}}{f}. \quad (1.2)$$

Note that in Figure 1.5 b) I represent the objective lens as a single element. This is a simplification.

In the paraxial limit ray-tracing calculations for a thick lens or even several consecutive lens elements can be simplified by bending the ray only at one place — at the principal plane.

Microscope objectives must collect light from a large aperture in order to produce a high resolution image. This is a fact I will support shortly using the wave-optical model. Unfortunately the large ray angles in the objective prevent its simplified description using principal planes, but an analysis using the eikonal theory (?) shows

1. Introduction

that an optical system that fulfills the Abbe sine condition allows perfect imaging even for widespread ray bundles.

$$\beta = \frac{n \sin \alpha}{n' \sin \alpha'} \quad (\text{Abbe sine condition}) \quad (1.3)$$

This condition ensures that the focal length, a quantity which is usually defined only for paraxial rays, is equal for all angles. This in turn means that such a lens carries out a Fourier transform from the front to the back focal plane with linear scaling. Note that a lens with a non-linear distortion in the back focal plane will fail to produce an image that is similar to the object.

aplanatic sphere

It turns out that ray bending in a high-aperture lens system that fulfills the Abbe sine condition can be simplified to a one bend at a single surface, quite similar to the utilization of principal planes in paraxial optics. For a high-aperture system this surface is no longer a plane. Instead it is a sphere with radius nf and called *aplanatic sphere*. I depict this surface as two circle segments with bold red strokes on the lenses in Figure 1.5 b).

In addition to the Abbe sine condition microscope lenses are also corrected for spherical aberration and linear coma (?). Then the coma rays are symmetric around the chief ray, the wavefront and point spread function are approximately invariant for small field sizes (in first order). This ensures that the imaging conditions are invariant for small regions of the field plane and allows to express image formation with linear systems theory.

1.3.2. Wave-optical theory for image formation in a fluorescence microscope

wave optics

In the following I want to describe how the image on the camera is formed. For this we have to use wave theory because close to the image rays intersect, invalidating ray-optical predictions. As both, wave-optical and ray-optical theory, are very much related, we can give a useful interpretation of the aplanatic surface for wave optics.

plane waves

The underlying Maxwell equations and the wave equation are linear and we can represent propagating solutions (evanescent solutions are neglected) of the wave equation as a superposition of the elementary solution — the monochromatic,

1. Introduction

plane waves described by wave vector \mathbf{k} :

$$u(\mathbf{r}, t) = u \exp(i(\mathbf{k}\mathbf{r} - \omega t)), \quad \mathbf{r} = (r_x, r_y, r_z), \quad \mathbf{k} = (k_x, k_y, k_z), \quad |\mathbf{k}| = 2\pi \underbrace{n/\lambda_0}_{1/\lambda}, \quad (1.4)$$

with vacuum wavelength λ_0 , refractive index n and wavelength λ in the immersion medium.

The accurate treatment of high-aperture optics would in fact require a vectorial calculation of the image for a fluorophore with a particular dipole orientation. Subsequently these images should be averaged to account for random fluorophore orientations, but as I do not need quantitative expressions I limit myself to the simpler scalar problem which provides qualitatively similar results.

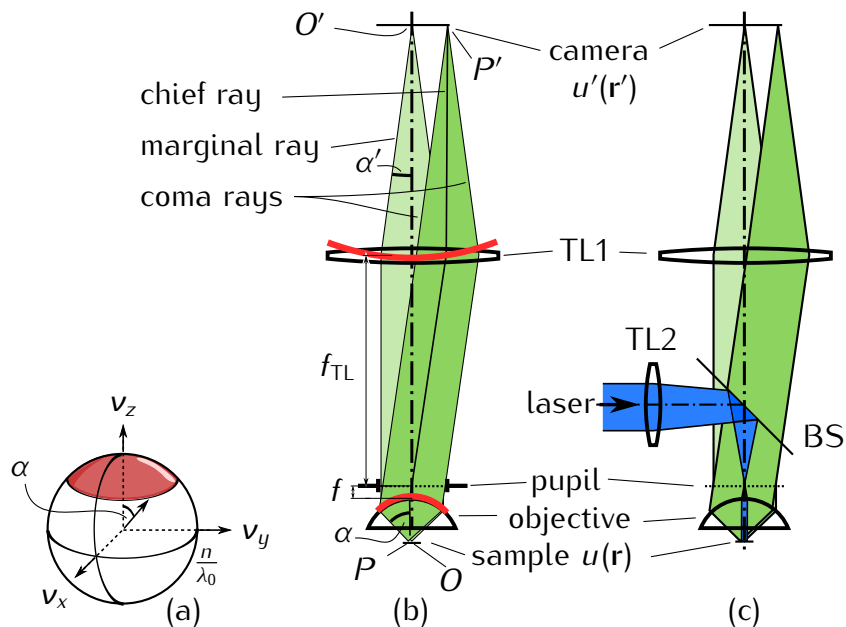


Figure 1.5.: a) Segment of the three-dimensional frequency spectrum of the light from the sample that is collected by the objective lens is highlighted in red on the Ewald sphere. b) Schematic of the detection path of a modern microscope. The sample is in the front focal plane of the objective. The detection tube lens TL_1 forms a magnified image on the camera. The aplanatic spheres for objective and tube lens are indicated in red. c) Parallel laser epifluorescence excitation. The excitation tube lens TL_2 focuses a laser into the pupil of the objective. The beam is reflected by a dichroic beam splitter (BS) towards the objective. An extended area in the specimen is illuminated. Fluorescence light returns through the objective, is transmitted through BS and forms an image on the camera.

widefield-microscope)

Ewald sphere

Assuming that the excited fluorophores in the sample give rise to a monochromatic

1. Introduction

electromagnetic field — I simplify the problem by omitting the complication that fluorophores emit photons in a wavelength range — then using the spatial frequency vector $\mathbf{v} = \mathbf{k}/(2\pi)$ we can expand the three-dimensional, stationary field amplitude distribution $u(\mathbf{r})$ into its spatial frequency spectrum $\tilde{u}(\mathbf{v})$:

$u(\mathbf{r}) :$	$\mathbb{R}^3 \rightarrow \mathbb{C}$	field distribution in sample space
$u'(\mathbf{r}') :$	$\mathbb{R}^3 \rightarrow \mathbb{C}$	field distribution in image space
$S(\mathbf{r}) :$	$\mathbb{R}^3 \rightarrow \mathbb{R}$	distribution of fluorophores in sample space
$I'(\mathbf{r}') :$	$\mathbb{R}^3 \rightarrow \mathbb{R}$	intensity distribution in image space
$\tilde{u}(\mathbf{v}) :$	$\mathbb{R}^3 \rightarrow \mathbb{C}$	spatial frequency spectrum of field in sample space
$a(\mathbf{r}) :$	$\mathbb{R}^3 \rightarrow \mathbb{C}$	amplitude point spread function
$\tilde{a}(\mathbf{v}) :$	$\mathbb{R}^3 \rightarrow \mathbb{C}$	amplitude transfer function, generalized aperture
$h(\mathbf{r}) = a(\mathbf{r}) ^2 :$	$\mathbb{R}^3 \rightarrow \mathbb{R}$	intensity point spread function
$\tilde{h}(\mathbf{v}) :$	$\mathbb{R}^3 \rightarrow \mathbb{C}$	optical transfer function

Table 1.1.: Overview of the functions that are used in this section.

:widedefield-functions>

$$u(\mathbf{r}) = \mathcal{F}(u(\mathbf{v})) := \int_{-\infty}^{\infty} \int_{-\infty}^{\infty} \int_{-\infty}^{\infty} \tilde{u}(\mathbf{v}) \exp(2\pi i \mathbf{r} \cdot \mathbf{v}) d^3 v \quad (1.5)$$

Where \mathcal{F} denotes the Fourier transform operation. I will use several functions in this section. See Table 1.1 for a listing of their names.

Since we have assumed a monochromatic field and the length $|\mathbf{v}|$ of the spatial frequency vector is the inverse of the wavelength (n/λ_0 , in the material of refractive index n), the support (denoted 'supp') of this spectrum $\tilde{u}(\mathbf{v})$ is limited to the surface of a sphere of radius n/λ_0 :

$$\text{supp } \tilde{u}(\mathbf{v}) = \{\mathbf{v} \in \mathbb{R}^3 : |\mathbf{v}| = n/\lambda_0\}. \quad (1.6)$$

This sphere is the transfer function of free space, and is also called Ewald sphere. Scaling the Ewald sphere with $f\lambda_0$ gives the aplanatic surface of the lens. Note that the x -component of the marginal ray (in the xz -plane) corresponds to the spatial frequency component $v_x = n \sin \alpha$ in object space and $v'_x = n' \sin \alpha'$ with $n' = 1$ in image space. The transversal spatial frequency components are related due to the Abbe sine condition (1.3):

$$\beta = v_x/v'_x, \quad \beta = v_y/v'_y. \quad (1.7)$$

The transfer function $\tilde{a}(\mathbf{v})$ of the lens is defined by complex values on the Ewald

1. Introduction

sphere (?):

$$\tilde{a}(\mathbf{v}) = P(\mathbf{v}_t) \exp\left(\frac{2\pi i}{\lambda} W(\mathbf{v}_t)\right) \delta\left(|\mathbf{v}| - \frac{n}{\lambda_0}\right) \text{step}(v_z), \quad (1.8)$$

$$\text{step}(x) = \begin{cases} 1 & x \geq 0 \\ 0 & x < 0 \end{cases}, \quad (\text{Heaviside step function}) \quad (1.9) \quad \text{eq:unit-st}$$

with the Dirac delta function δ , transversal spatial frequency vector $\mathbf{v}_t = (v_x, v_y)^T$, and the real valued pupil function $P(\mathbf{v}_t)$ and wavefront error $W(\mathbf{v}_t)$. McCutchen calls the three-dimensional function $\tilde{a}(\mathbf{v})$ the generalized aperture.

For this discussion I set $W(\mathbf{v}_t) = 1$, i.e. there is no wavefront aberration and the lens is diffraction limited. Furthermore, I use a uniform, solid cylinder as pupil function $P(\mathbf{v}_t)$ in order to limit the size of the calotte (or cap) of the Ewald sphere that is defined by the acceptance angle α of the objective²:

$$P(\mathbf{v}_t) = \text{step}\left(|\mathbf{v}_t| - \frac{n \sin(\alpha)}{\lambda_0}\right), \quad (1.10)$$

with the Heaviside step function as defined in equation (1.9). In general $P(\mathbf{v}_t)$ can assume values between 0 and 1 in order to account for apodization due to natural vignetting or angle-dependent Fresnel reflection losses on the lenses. I ignore such effects in this discussion. Also, just as the objective lens, the tube lens can be described by its generalized aperture but I assume that the tube lens maintains a diffraction limited wavefront of the full angular range. For this discussion, the full microscope is readily described by the generalized aperture of just its objective lens.

Multiplication of the angular frequency spectrum $\tilde{u}(\mathbf{v})$ with the generalized aperture $\tilde{a}(\mathbf{v})$ gives the angular frequency spectrum of the amplitude in the image:

$$\tilde{u}'(\mathbf{v}') = \tilde{u}'(\mathbf{v}/\beta) = \tilde{u}(\mathbf{v}/\beta) \cdot \tilde{a}(\mathbf{v}/\beta). \quad (1.11)$$

Note that I use the transversal magnification β to scale the arguments of the functions, so that the result is given in image space spatial frequencies³.

²Note that this expression is only valid for $\alpha \in [0, \pi/2]$. An expression for $\tilde{a}(\mathbf{v})$ encompassing the full range $[0, \pi]$ for α must contain two functions of each P and W , in dependence on whether the spatial frequency vector \mathbf{v} is directed in or against the direction of the optical axis. This is necessary to express the transfer function of a 4Pi or I^nM microscope.

³Unfortunately my notation is slightly problematic here. I assume that z-sampling occurs by stepping the sample through the object space while the camera is fixed in the focal plane of

1. Introduction

According to the convolution theorem this multiplication in frequency space corresponds to a convolution in the domain of spatial coordinates \mathbf{r} of the field distribution $u(\mathbf{r})$ and an amplitude point spread function $a(\mathbf{r}) = \mathcal{F}(\tilde{a}(\mathbf{v}))$ that describes the imaging of the objective lens:

$$u'(\mathbf{r}') = u'(\beta\mathbf{r}) = (u \otimes a)(\mathbf{r}) = \int_{-\infty}^{\infty} \int_{-\infty}^{\infty} \int_{-\infty}^{\infty} u(\boldsymbol{\varrho}) a(\mathbf{r} - \boldsymbol{\varrho}) d^3\boldsymbol{\varrho} \quad (1.12)$$

where $\boldsymbol{\varrho}$ is a spatial coordinate and the lateral magnification $\beta = \mathbf{r}'/\mathbf{r}$ transforms between image space \mathbf{r}' and object space \mathbf{r} . This result shows that the three-dimensional amplitude distribution of the image is linearly related to the amplitude distribution in the sample.

A focal plane detector can only measure the intensity I' which depends non-linearly on the amplitude of the field u' . However, the fluorophores act as independent sources and their phases vary randomly with respect to each other. Each fluorophore gives rise to its coherent image $h(\mathbf{r}')$ (?):

$$h(\mathbf{r}') = |a(\mathbf{r}')|^2. \quad (1.13)$$

The three-dimensional intensity distribution $I'(\mathbf{r}')$ in image space can then be obtained by incoherently adding the individual images of the fluorophores:

$$I'(\mathbf{r}') = \int_{-\infty}^{\infty} \int_{-\infty}^{\infty} \int_{-\infty}^{\infty} S(\boldsymbol{\varrho}) h(\mathbf{r}' - \boldsymbol{\varrho}) d^3\boldsymbol{\varrho} \quad (1.14)$$

$$= (S \otimes h)(\mathbf{r}') \quad (1.15)$$

where $S(\boldsymbol{\varrho})$ represents the three-dimensional fluorophore distribution and $\boldsymbol{\varrho}$ is the spatial coordinate in image space.

It is useful to discuss the Fourier transform of the intensity point spread function h . This is the three-dimensional optical transfer function of the microscope and describes how well different spatial frequencies are transmitted:

$$\tilde{h}(\mathbf{v}') = \mathcal{F}(a(\mathbf{r}') a^*(\mathbf{r}')) = \tilde{a}(\mathbf{v}') \otimes \tilde{a}^*(-\mathbf{v}'). \quad (1.16) \boxed{\text{eq:otf}}$$

The product of the amplitude point spread function $a(\mathbf{r}')$ and its complex conjugate corresponds to an auto-correlation of the amplitude transfer function in spatial frequency space. Note that the complex conjugation of the second factor $a^*(\mathbf{r}')$ results in an inversion of the argument of $\tilde{a}^*(-\mathbf{v}')$.

the tube lens. Therefore the axial coordinates r_z and r'_z in object and image are identical.

1. Introduction

This expression allows a geometric interpretation of the support of the optical transfer function $\tilde{h}(\nu)$ (?). Equation (1.16) describes a convolution of two spherical caps whose open sides are facing each other. The entire covered volume somewhat resembles a torus with vanishing internal diameter. Figure 1.6 depicts a $\nu_x\nu_z$ -cross-section for two different aperture angles α . The lateral $\Delta\nu_x$ and

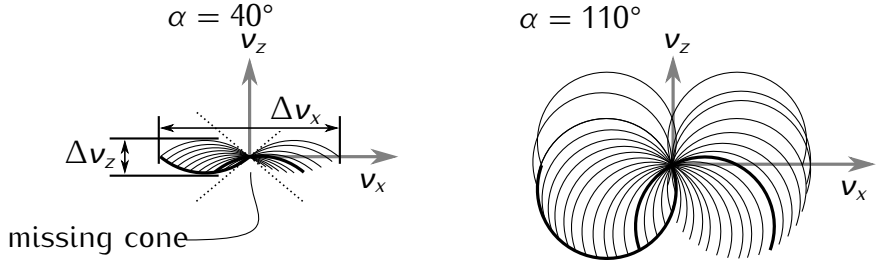


Figure 1.6.: Schematic depicting $\nu_x\nu_z$ -cross sections of the support of optical transfer function \tilde{h} for microscope objectives with different collection angles. **left:** Objectives, that only collect light that is directed into one half space, have the missing cone problem. **right:** Optical transfer function for fictional objective with larger collection angle and no missing cone.

`{fig:missing-cone}`

axial $\Delta\nu_z$ extent of the optical transfer function can be expressed in terms of wavelength λ_0 , immersion index n and aperture angle α :

$$\Delta\nu_x = \begin{cases} 4n \sin(\alpha)/\lambda_0 & 0 \leq \alpha \leq \pi/2 \\ 4n/\lambda_0 & \pi/2 < \alpha < \pi \end{cases}, \quad \Delta\nu_z = 2\frac{n}{\lambda_0}(1 - \cos \alpha), \quad (1.17)$$

resolution

(FIXME verify with rainers book chapter) allow to give lower bounds for the resolution that can be obtained using a well corrected objective:

$$\Delta d_x = \frac{2}{\Delta\nu_x} = \frac{\lambda_0}{2n \sin \alpha}, \quad \Delta d_z = \frac{2}{\Delta\nu_z} = \frac{\lambda_0}{n(1 - \cos \alpha)}. \quad (1.18) \quad \text{[eq:resolut]}$$

In order to sample the bandwidth limited signal in the image plane correctly, the pixel pitch p_x of the camera must be smaller than half of the resolution: $p_x < \beta\Delta d_x/2$ (Nyquist criterium). A similar relation holds true for the z -sampling: $p_z < \Delta d_z/2$. Too large a sampling period will result in aliasing artifacts.

Note that the axial resolution Δd_z is substantially worse than the lateral resolution Δd_x in normal microscope with a collection aperture $\alpha < \pi/2$ that is restricted to only one half-space.

Additionally the optical transfer function of such a microscope is empty in a cone shaped region around the axis above and below the origin. This means

1. Introduction

that in a conventional wide-field microscope it is impossible to bring into focus a (defect-free) fluorescent plane because low spatial frequencies do not attenuate with defocus (?). This effect is also called “missing cone problem” (?).

It is instructive to look at a microscope, that is not hampered by the missing cone problem: In image interference microscopy (I^2M) two opposing microscope objectives collect light from the sample and the two detection beam paths are brought to interference using a beam splitter on a focal plane detector. This configuration substantially increases the collection angle, improves the z -resolution and fills the missing cone but puts stringent requirements on the optical path difference between the two interferometer arms, i.e. this device is very sensitive to sample-induced aberrations and in practice, with fluorophores that emit in a broad wavelength range, this method only works for samples which are only a few microns thick (Gustafsson et al. 1999).

Light from the focal plane interferes constructively on the detector, light emitted at $\lambda/4$ distance away from the focal plane interferes destructively, light that is emitted at several wavelengths distance from the focal plane contributes as an incoherent sum to the detected signal. Therefore a z -stack of a fluorescent plane captured with two opposing lenses compared to just one lens will give a signal that is four times as bright in focus, shows damped oscillations (because of the finite spectral band emitted by the fluorophores) when going away from focus and has twice the brightness out-of-focus. This means the axial location of the fluorescent plane can be measured in I^2M but there is still background signal (?).

The reason for this background signal is conservation of energy from plane to plane. A light ray that started in a certain object point does not stop in the corresponding image point. Therefore most out-of-focus light is added incoherently as a background to the detected signal. Structured illumination can be used to remove this out-of-focus light (?) (FIXME reference to confocal and structured illumination sections).

1.3.3. Illumination in a wide-field epifluorescence microscope

As mentioned in section 1.2, fluorescence photons are essentially emitted in all directions by a typical, (nearly) independent of the original illumination direction. Therefore it is possible and convenient to use the objective for excitation as well as detection. This mode of microscopy is called epifluorescence (Greek: $\varepsilon\pi\iota$; on, above). In this configuration usually only a small percentage of the excitation light returns due to scattering or reflection. This simplifies the separation of

1. Introduction

fluorescence light from excitation light and parts of opaque specimen can be imaged.

The blue beam in Figure 1.5 c) depicts a parallel laser that is focused into the pupil of the objective by tube lens TL2. The beam is reflected at a dichroic beam splitter (BS). This is a glass plate that has been coated with dielectric layers. The refractive index, thickness and sequence of the layers are designed so that the excitation light is reflected towards the objective. Excitation light, that is scattered or reflected in the sample and returns through the objective is reflected towards the light source. However, lower energy fluorescence light returning from the objective is transmitted towards the camera. Behind the objective the beam is parallel and illuminates the specimen. The field of view is the demagnified diameter of the laser beam before TL2.

Non-uniformity due to coherent interference

Note that tiny dirt particles in the excitation beam path can cause coherent interference and produce unwanted non-uniformities in the illumination. As a remedy the spatial coherence of the laser is sometimes reduced. Incoherent light emitting diodes, mercury or xenon arc lamps are often used instead of lasers. In the latter case a band pass filter selects the useful part of the spectrum of the excitation lamp upstream of the dichroic beam splitter.

The space-bandwidth product of a microscopic lens

etendue (sec:etendue) A useful quantity in optics is the etendue \mathcal{E} . For a microscope objective its value is related to the number of point spread functions that can be resolved in the field. Therefore this quantity is also called information capacity, light gathering capacity or space-bandwidth product. For a high-aperture lens, the etendue is given by

$$\mathcal{E} = \frac{\pi}{4} (D_{\text{field}} \text{NA})^2, \quad (1.19) \text{ ?eq:high-ap}$$

with the numerical aperture NA and the field diameter D_{field} . The typical image diameter for Zeiss microscopes is 25 mm. For a 63 \times oil-immersion objective with NA = 1.4 this corresponds to a field diameter of $D_{\text{field}} = 0.4$ mm and an etendue of $\mathcal{E} = 0.27 \text{ mm}^2/\text{sr}$, where 'sr' denotes steradian, the SI unit of solid angle.

1. Introduction

1.3.4. Phototoxicity in conventional microscopes

When imaging living specimen we should distinguish between useful and unnecessary excitation. Taking into account the detection capabilities of objective lenses we should maximize the ratio of in-focus to out-of-focus fluorescence. The epifluorescent wide-field and confocal microscope surely do not represent an optimum in this regard.

In chapter ?? I will introduce other microscopy techniques that are more considerate of where to deposit excitation power within the specimen.

1.3.5. Conclusion

?idefield-conclusion)? In this section I introduced a theoretical model that describes image formation in a wide-field microscope. For well-corrected, diffraction-limited lenses this process is linear in intensity and three-dimensionally shift-invariant. In order to predict the image of a three-dimensional sample it is sufficient to know the image of a single point source.

By investigating this point spread function and its Fourier transform it is possible to give the simple relationships in equations (1.18) for the best possible resolution. Furthermore I describe the missing cone problem, a limitation inherent in all lenses that only collect light from one half-space.

1.4. Image detectors in wide-field microscopy

?<sec:ccd-intro)?

I describe the operation of CCD, EM-CCD and sCMOS focal plane detectors. Then I utilize a simple noise model to compare different camera models and describe a simple method to calibrate cameras so that their data is represented in the standardized unit of detected photoelectrons.

1.4.1. Introduction

detection

Nowadays, all wide-field microscopes use silicon-based cameras to measure and digitize the intensity distribution in the intermediate image plane. The semiconductor surface is patterned with a two-dimensional array of PIN photodiodes that generate and collect an intensity-dependent amount of free charge carriers when their depletion region is exposed to light photons.

quantum efficiency
and back-thinning

Modern detectors can have a very high probability of a photon being absorbed and contributing to final signal (quantum efficiency Q_E). For the most light

1. Introduction

sensitive devices even the backside of the silicon substrate is removed until the diodes can be exposed from the backside. In this way, the diodes can cover the entire surface and the fill factor is not reduced due to opaque wires running over the surface. Such detectors are called 'back-thinned' and can achieve a quantum efficiency of up to 95% for green light.

There are basically two different technologies to measure and digitize the charge that was collected in the photodiodes:

In the passive-pixel sensor columns of diodes form a linear row of capacitors. By applying a sequence of different voltages, in the range up to 6 V to each of three adjacent capacitors, the charge can be transported line by line out of the sensor — therefore, this technology is known as charge-coupled device (CCD). An additional row of similar capacitors (denoted horizontal shift register) on one side of the array pushes the carriers into a charge amplifier. This consists of a much smaller capacitor (the read node) and a field-effect transistor that amplifies the voltage across the read node. This voltage linearly depends on the charge (?).

In the active-pixel sensor each individual photodiode is surrounded by its own transistors for readout and reset. The two-dimensional array is addressed with an access enable wire which is shared by pixels of a line and an output wire, which is shared by pixels of a column. In the simplest case (with three in-pixel transistors) start of integration and readout occurs one line at a time (rolling shutter).

When I started this work in 2008, passive CCD sensors were state of the art detectors for fluorescence microscope with regards to sensitivity and speed. Now, however, faster and cheaper active-pixel sensors that provide comparable or better noise performance, become commercially available.

In the next section I will deal with various noise sources that affect the signal of focal plane detectors. This is not only relevant to compare the performance of cameras from different manufacturers or to determine the optimal parameter settings for one particular experiment; often it is advantageous to specify an intensity measurement as the number of detected photoelectrons, e.g. when comparing images of different microscope systems (confocal, spinning disk or wide-field) or when utilizing sophisticated noise reduction algorithms.

1.4.2. Photon shot noise and read noise

Fluorescence photons arrive at the detector independently of each other. This random process leads to fluctuations in the number of the detected photons and

Charge-coupled
devices (CCD)

charge amplifier

active-pixel sensor

Photon shot noise

1. Introduction

can be described by the Poissonian probability mass function (denoted as 'pois'):

$$\text{pois}(k; \lambda) = \frac{\lambda^k \exp(-\lambda)}{k!}, \quad \lambda \in \mathbb{R}, \quad k = 0, 1, 2, \dots \quad (1.20)$$

Note that in this particular formula the quantities have a different meaning than in other parts of this work. The variable k describes the number of measured photons and the real number λ is the average number of photons that reach the detector during the integration time. Figure 1.7 displays the discrete detection probabilities for three different values of λ .

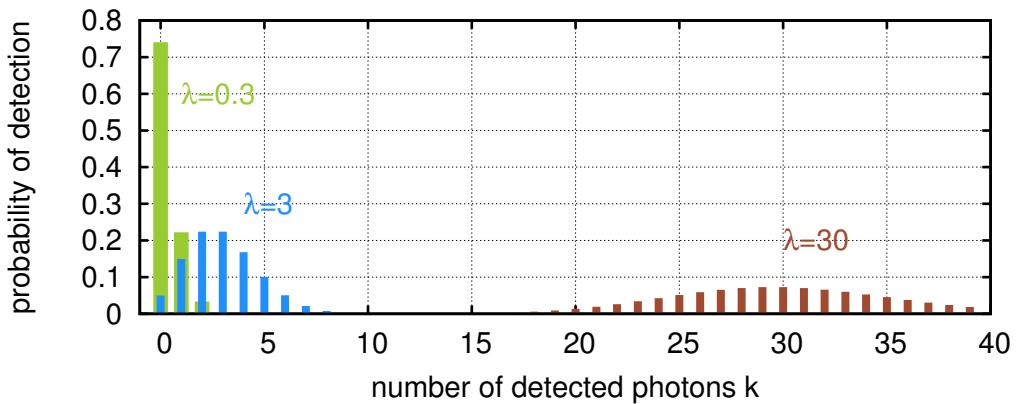


Figure 1.7.: Poissonian probability mass function $\text{pois}(k; \lambda)$ for three photon fluxes with different average photon numbers λ .

`{fig:pois}`

We can calibrate every detector in order to specify the measurement in the unit of detected photoelectrons. For this, we utilize the property of the Poisson distribution that the variance $(\Delta I)^2$ of an intensity measurement (in the unit of photoelectrons) is equal to the average intensity $\langle I \rangle$:

$$(\Delta I)^2 = \langle (I - \langle I \rangle)^2 \rangle = \langle I \rangle. \quad (1.21) \quad \boxed{\text{eq:variance}}$$

detector gain calibration

For the calibration of a detector, twenty images of a defocused fluorescent object (see left image in Figure 1.8) are acquired. From the twenty images the variance of the intensity is determined for each pixel. Then all occurring intensities are collected into 100 bins. The average intensity variance of each bin is then plotted against the intensity (see right image in Figure 1.8). The data lie on a straight line. From its slope we calculate the gain to convert the arbitrary analog-to-digital units into the number of detected photoelectrons. If the data is plotted in this unit, the slope of the line is one, according to equation (1.21). The smooth light distribution in the input images ensures a good coverage for each data point in

1. Introduction

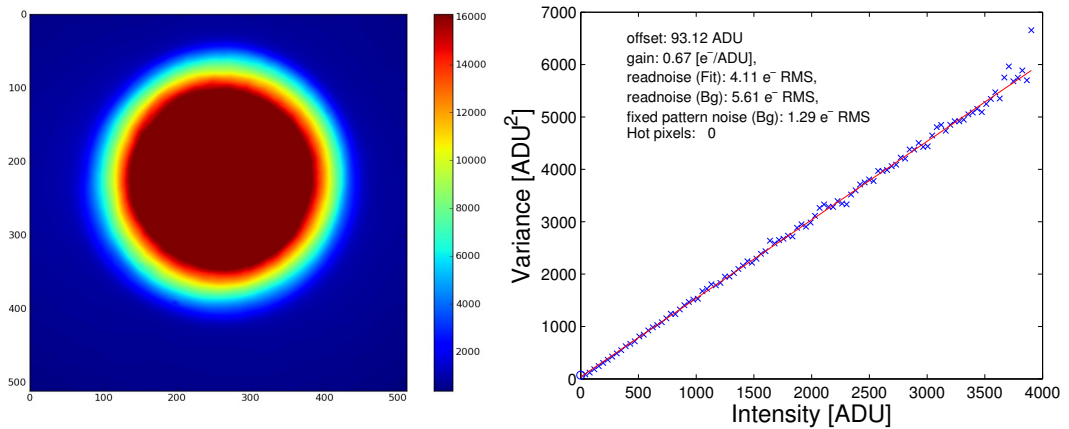


Figure 1.8.: **left:** Image of a defocused area on a fluorescent plane sample. This is used for calibrating the detector. **right:** Result of a detector calibration. The slope of the curve allows to convert the arbitrary analog-to-digital units into detected photoelectrons, the point of interception at the y -axis gives the detector read noise.

`(fig:shot-noise)`

the variance-intensity plot.

`measuring read noise`

To determine the quality of a detector we ensure that no light falls on the detector and create twenty dark images. For an ideal, noise-free detector these images would contain zero everywhere. In a real CCD sensor the variance of the values in the dark images reflect the readout noise N_r . Using the calibration gain, the readout noise can be specified as photoelectrons/pixel (e/px).

The analysis for the right diagram in Figure 1.8 gave a readout noise of 5.6 e/px. For the evaluation I used the function `cal_readnoise` of the DIPimage toolbox for Matlab (?). In appendix A.2 I list an alternative Python implementation of this algorithm.

The major source for readout noise is the charge amplifier. Its noise is added uniformly to every image pixel. For readout frequencies above 1 MHz the readout noise increases with the square root of the read speed (?). Until a decade ago this limited the readout speed of scientific CCD cameras. Then a new type of sensor was developed — the electron-multiplying CCD (EM-CCD) (?).

`electron-multiplying
CCD`

This device contains an additional sequence of capacitors (denoted multiplication registers), which are operated with a high voltage (up to 46 V). The field accelerates electrons and they can generate more charge carriers by a process called impact ionization. This is a statistical process and for every electron going through a multiplication register, there is an average probability p that it creates another electron. This probability is quite low ($p < 1.3\%$) but after a sequence of 536

1. Introduction

registers the gain $M = (1 + p)^{536} \approx 1015$ is so high, that even readout noise at 17 MHz readout speed can be neglected.

This amplification process consumes a lot of energy and requires an elaborate cooling scheme of the detector chip as the gain is temperature dependent.

Unfortunately, the statistical nature of impact ionization leads to an uncertainty in gain and therefore introduces a new noise source. As a gain this noise acts multiplicatively on the signal. ? analyzed the amplification process and shows that the multiplicative noise, which is also called excess noise, has the effect of halving the apparent quantum efficiency of the detector.

Note that for very low light conditions with a minute probability to detect more than one photon per pixel, the EM-CCD can be run with maximum gain as a binary detector in photon counting mode. In this mode the excess noise has no effect whatsoever; but other noise sources become important.

1.4.3. Comparison chart for detector selection

Now I will introduce a comparison chart that I first saw in ?. It is based on a single formula for the signal-to-noise ratio SNR and if the detector parameters, such as readout noise and quantum efficiency, are known, a quantitative estimate of the expected quality of the data can be made.

Shot noise defines the fundamental limit for the signal-to-noise ratio in photo detectors (?). As already mentioned above, the expected noise for a signal of S photons is \sqrt{S} . Assuming the contributions to a detector pixel are S photons signal perturbed by an additional number of I_b photons background light. The signal-to-noise SNR_{id} ratio for an ideal, noise-free detector is:

$$\text{SNR}_{id} = \frac{S}{\sqrt{S + I_b}}. \quad (1.22)$$

A conventional detector with reduced quantum efficiency $Q_E \in [0, 1]$ and additive readout noise N_r (in e/px) can only produce a worse signal-to-noise ratio:

$$\text{SNR}_{add} = \frac{Q_E \cdot S}{\sqrt{Q_E(S + I_b) + N_r^2}}. \quad (1.23)$$

This formula can be adapted for the electron-multiplying CCD. There, the readout noise is reduced because of the gain M but the influence of the shot noise is

excess noise reduces quantum efficiency

1. Introduction

doubled due to the excess noise factor $F_n = \sqrt{2}$.

$$\text{SNR} = \frac{Q_E \cdot S}{\sqrt{F_n^2 \cdot Q_E \cdot (S + I_b) + (N_r/M)^2}} \quad (1.24)$$

This equation makes it possible to compare all the cameras that I can use for my experiments. Table 1.2 lists parameters from their datasheets and the three diagrams in Figure 1.9 shows curves of the relative signal-to-noise ratio $\text{SNR}/\text{SNR}_{id}$ for three different amounts of background light I_b .

When choosing the parameters I attached particular importance to the noise performance, even if that comes with a loss in readout speed.

camera type	f_{read} [MHz]	QE	N_r [e/px]	F_n	M	model
back-thinned CCD	1	0.95	5.3	1	1	E2V CCD97
EM-CCD	1	0.95	15.0	$\sqrt{2}$	80	E2V CCD97
EM-CCD single photon	17	0.95	89.0	1	1000	E2V CCD97
sCMOS global shutter	200	0.52	2.3	1	1	Fairchild CIS2521F
sCMOS rolling shutter	140	0.72	1.3	1	1	Hamamatsu FL-400
back-thinned sCMOS	—	0.95	0.7	1	1	— ⁴
interline CCD	20	0.62	6.5	1	1	Sony ICX285
interline CCD	1	0.62	2.4	1	1	Sony ICX285

Table 1.2.: Camera parameters for the curves in Figure 1.9.

`(tab:cam-param)`

For a very large number of photons the detector with the highest quantum efficiency QE wins (back-thinned CCD, green line):

$$\lim_{S \rightarrow \infty} \frac{\text{SNR}}{\text{SNR}_{id}} = \frac{\sqrt{Q_E}}{F_n}. \quad (\text{high light limit}) \quad (1.25)$$

For detectors with readout noise, there is a signal photon number S_n below which the readout noise predominates:

$$S_n = \frac{N_r^2}{M^2 F_n^2 Q_E} - I_b. \quad (\text{photon shot noise limit}) \quad (1.26)$$

I indicate both limits in Figure 1.9 using different line types. The line is dotted in the region where the readout noise dominates, followed by a thick solid line where both photon shot noise and readout noise contribute. A thin line indicates the region where the relative SNR is within 95% of the high light limit and the sensor's quantum efficiency becomes the parameter that defines the performance.

⁴Back-thinned sCMOS are not available at the time of writing.

1. Introduction

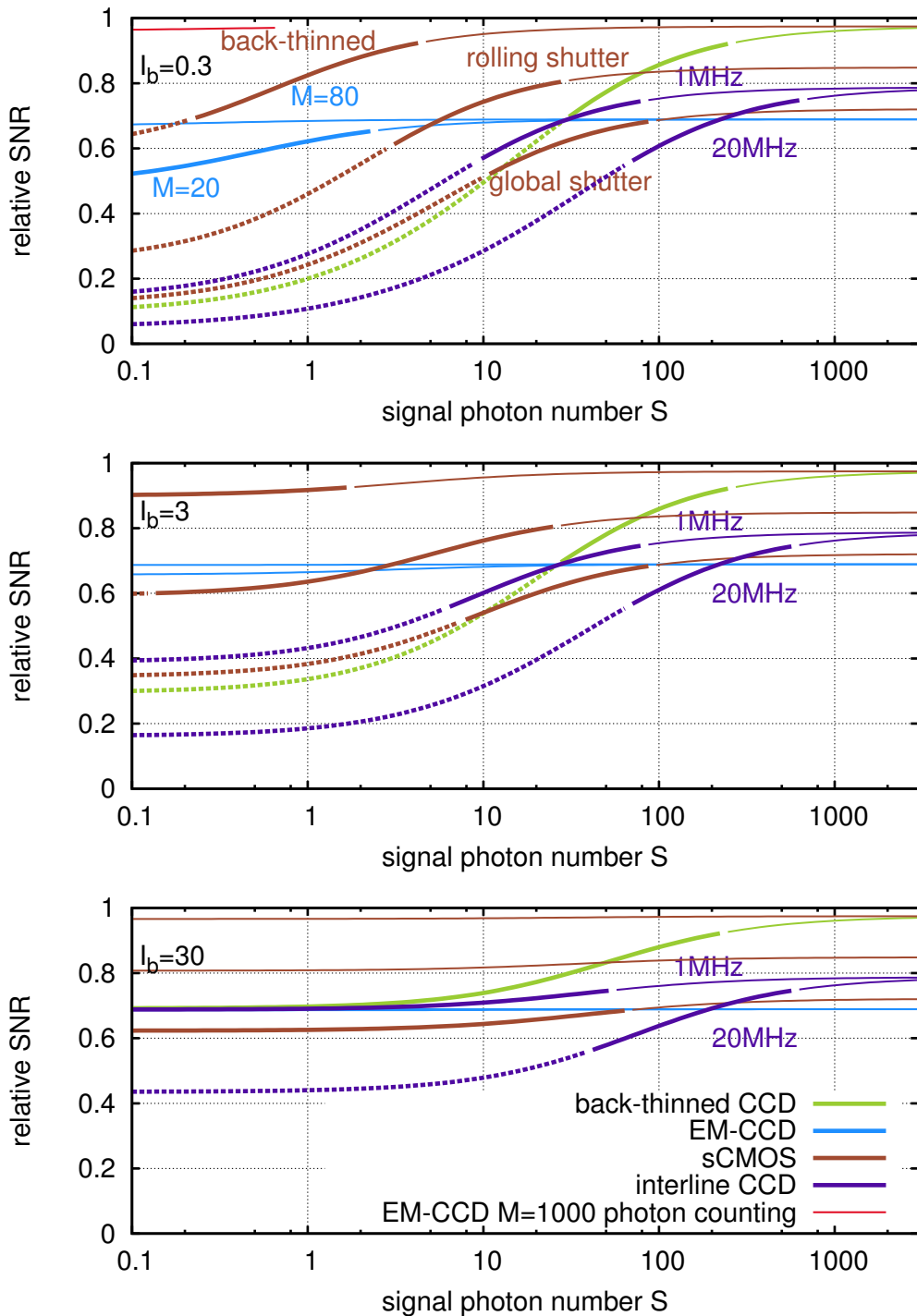


Figure 1.9.: Camera snr. dotted line for lowest light level, where N_r is the dominant noise; thin line indicates high light region where quantum efficiency and excess noise factor F_n matter

(fig:camera-snr)

interpretation of
EM-CCD in Figure 1.9

The first thing I want to look at is the EM-CCD. For a high gain of $M = 20$ the curve is horizontal and the sensor differs from the ideal detector only in terms of

1. Introduction

a reduced apparent quantum efficiency. In a low background environment $I_b = 0.3$ the electron multiplying mode is only advantageous for signals with less than 30 photons per pixel. For a higher background $I_b = 30$ electron multiplication does not improve noise performance — but note that in this mode the sensor could be read out at a 10 times higher speed.

In a low background environment and low signal level the EM-CCD comes very close to the ideal detector, when it is run in photon counting mode as indicated by the red line in the top left.

sCMOS in Figure 1.9

Next I want to discuss the curves of the active-pixel sensors.

The device designated as global shutter sCMOS is a sensor with five transistors per pixel (?). Similar to a passive-pixel CCD sensor this permits to start exposure in all pixels simultaneously, but it has two major drawbacks. The additional two transistors cover space that would otherwise be available as light sensitive area and for quantitative data, a reference frame must be taken for each image, which increases the readout noise (??).

The rolling shutter sCMOS sensor has only the minimum three transistors per pixel and therefore a correspondingly higher quantum efficiency. For a signal between 6 and 80 electrons per pixel this sensor provides the best quality at 8 times higher readout speed than the EM-CCD. Rolling shutter means that the pixel lines are read in succession but for our prototype it is crucial that all pixels integrate while the displays show patterns. Fortunately there is a mode called global exposure synchronization which initiates integration in the pixels line by line and generates a trigger output once all pixels have started capturing light. This allows to use the camera as a master without further effort but the camera can also be run as a slave. In that case the only requirement is that the trigger comes early enough (10 ms, ?) to initiate exposure in all lines before the illumination is activated.

The entry back-thinned sCMOS is only a hypothetical sensor which I added to compare the performance of a low noise activ-pixel sensor with near perfect quantum efficiency.

1.4.4. Calibration of the EM-CCD gain

The method I presented for CCD calibration can be applied to measure the gain M and the excess noise factor F_n of an EM-CCD. This requires dark images and image sequences of the smooth intensity distribution (from the exactly the same sample) with and without electron multiplication gain, so that data for both cases

1. Introduction

can be converted into detected photoelectrons.

The apparent quantum efficiency with gain is Q_E/F_n . Therefore the excess noise factor can be calculated with

$$F_n = N_{(1)}/N_{(M)} \quad (1.27)$$

where $N_{(1)}$ and $N_{(M)}$ are the sum of photoelectrons in the image without and with electron multiplication gain, respectively.

The variance for data without gain is $(\Delta I)_{(1)}^2 = Q_E \langle I \rangle$ and smaller than for data with gain, where the variance is $(\Delta I)_{(M)}^2 = Q_E F_n^2 \langle I \rangle$.

The x -axis in the intensity-variance plot is equal to the intensity for gain-free data and scaled with M for the amplified data. The gain M can be calculated from both slopes $m_{(1)} = Q_E$ and $m_{(M)} = Q_E F_n^2 / M$ of the intensity-variance curves:

$$M = F_n^2 \frac{m_{(1)}}{m_{(M)}}. \quad (1.28)$$

In appendix A.1 I show code to automatically measure data for this calibration. In order to cover a large span of gains, I capture a short exposure image before each measurement and adjust the exposure time such that the sensor is never overexposed.

Table A.1 summarizes the calibration results. The average of the dark images (in ADU) is given in the column offset. The read noise in conventional mode is approximately 8 electrons per pixel rms. The column mean' contains the average number of photoelectrons per pixel in the illuminated image normalized by the integration time. The rows conv1 and conv2 with conventional readout (without EM-gain) contain approximately the same number. This proves that no significant bleaching occurred during the experiment.

1.4.5. Conclusion

In this section I discussed how various camera sensors work. I have explained photon shot noise, which follows from the quantum mechanical nature of light and so far constitutes a fundamental limit of light detection. Based on this, I explained a calibration method that helps to evaluate camera performance and, maybe more relevant for this work, allows to compare images that were created with different microscopes.

Since low-noise active-pixel cameras became available only late during my project, and the first models still had some issues — unstable software or in

1. Introduction

the case of the Hamamatsu Orca Flash 2.8 too few outputs for trigger signals, I designed my system for EM-CCD. For most experiments, however, I used an interline CCD.

2. Methods of controlling illumination patterns

<sec:illum-patterns> 2.0.6. 2-photon laser scanning fluorescence microscopy

?<sec:2-photon>? If the laser intensity in the focal spot of a confocal microscope is sufficiently high, then two infrared photons can be absorbed within $\sim 5\text{ fs}$ and excite the same electronic state.

In this regime, the fluorescence emission increases quadratically with laser intensity. This non-linearity confines the excitation volume to the vicinity of the focal plane (Denk et al. 1990). Fluorophores outside of this region are not excited. Therefore this method produces sectioned images by default and there is no need for a detection pinhole.

As an additional benefit infrared light is scattered less than visible light of half the wavelength. This increases penetration depth and image quality. Photodamage outside of the focal volume is unlikely and phototoxicity is much lower, compared to the single-photon confocal microscope, when z-stacks are acquired.

However, the phototoxicity within the focal volume is higher and techniques like ultramicroscopy (section ??) with single-photon excitation are preferable, when low overall phototoxicity is a requirement.

2.1. programmable array

Caarls et al. (2011)

3. The concept of spatio-angular microscopy

?<sec:concept> Here I introduce the spatio-angular microscope. First I explain the concept of its illumination system using exemplary fluorophore distributions, that occur in typical specimen.

Then I describe some decisions we faced during the initial design phase concerning the arrangement of optical components. Furthermore, I position our method among known approaches of light control for microscopy. Of all published techniques for excitation illumination control, the light field microscope (Levoy et al. 2006) comes closest to our approach. I explain differences between both techniques and discuss their respective pros and cons. I address the peculiarities and limitations of the hardware components in chapters 4 (optics) and ?? (micromirror based pupil plane SLM). Initially, the details would be detrimental to clarity.

The effective use of the spatio-angular microscope, requires more knowledge about the specimen than a conventional or a SPIM microscope (Huisken et al. 2004). Ideally, the distribution of refractive index and fluorophores in the specimen should be known. If these parameters were precisely known, there would be no need for an image in the first place. However, while imaging a known specimen, sufficiently good predictions of these parameters can often be made. The higher the accuracy of these prognoses, the greater the reduction in phototoxicity will be.

The computer-based selection of appropriate illumination masks requires the prediction, or at least an approximate estimation, of the three-dimensional distribution of light in the specimen.

In the last part of this chapter, I describe the computational control loop in our spatio-angular microscope and touch topics of image processing.

3.1. Motivation

In order to introduce the basic idea underlying the spatio-angular microscope, I consider the distribution of excitation light in the object of a conventional

3. The concept of spatio-angular microscopy

fluorescence microscope: Figure 3.1 a) schematically illustrates the side view of the excitation beam path through objective lens and object in a confocal microscope. A parallel beam with a circular cross-section (this cross-section is not shown in the illustration) passes through the lens. The lens focuses the light in its focal plane.

Between lens and focal plane the light rays form a convergent circular cone. If refractive index variations in the object are negligible, the light distribution below the plane of focus forms a cone as well, due to symmetry. Assuming a non- or weakly absorbing specimen, the energy of the light in the circular cross-sections of the cone remains constant¹.

(sec:ray-valid) The fluorescent bead (1), in the focus, would therefore be excited significantly more than the bead (2) outside the focal plane. Also shown is the light distribution in the intermediate image plane.

The image of the in-focus bead (1) is sharp, i.e. its emanating fluorescence light is concentrated on an area as small as possible and positioned exactly on the detection pinhole. Conversely, the image of the out-of-focus bead (2) is blurred and its fluorescence light is distributed over a large area.

While only a tiny proportion of the light emitted by the out-of-focus bead contributes to the detection signal of the confocal microscope—and therefore hardly affects the image quality, with respect to overall phototoxicity of the full confocal system—it would be better to prevent the excitation of the out-of-focus bead in the first place.

The scheme in Figure 3.1 b) demonstrates how the light cone would have to be manipulated in order to exclude the out-of-focus bead (4). The expected fluorescence image in the intermediate image plane then contains only information from the in-focus bead (3).

Viewed from the in-focus bead (3) the change in illumination corresponds to a restriction of the light angles. Such control can be exerted well through a mask in the other focal plane of the objective lens (also denoted back focal plane or pupil plane).

¹The ray-model is valid in large parts of Figure 3.1 a), but not everywhere. The Law of Malus–Lupin states that rays and wavefronts are equivalent as long as rays do not intersect (caustic), or (FIXME formulas?) a strong intensity gradient occurs. Thus the ray-model is valid almost everywhere in the cone, except for a region with a distance of a few wavelengths to the edge, and the focus itself. While the wave-optical treatment of these areas is possible, it is computationally much more expensive than ray tracing. Wave-optical effects either lead to blurring in a length scale of a few wavelengths or intensity fluctuations due to interference. If necessary, we can use heuristics to find an upper bound for the local intensity from ray tracing results. For this reason we exclusively employ the ray-model in this work.

3. The concept of spatio-angular microscopy

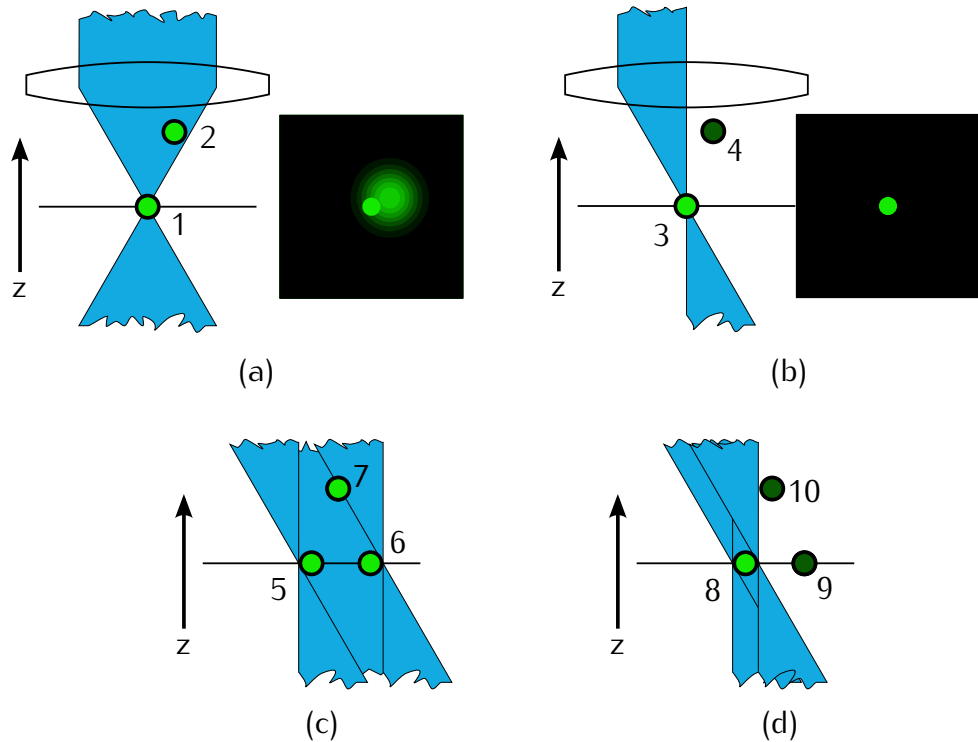


Figure 3.1.: (a) Two fluorescent beads are illuminated by all angles that the objective can deliver. The sharp image of the in-focus bead is deteriorated by blurry fluorescence of the out-of-focus bead (2). (b) Angular control allows selective illumination of the in-focus bead (3), and results in a better image on the camera. (c) Angular control, however, is insufficient, when an extended in-focus area is illuminated. (d) Then, simultaneous spatial and angular control allows sequential excitation of the in-focus beads, while excluding the out-of-focus bead (10).

`<fig:hourglass-all>`

Thus it is useful and possible to equip a confocal microscope with angular control. However, in our project we set out to build a wide field microscope in order to benefit from the speed and quantum efficiency of modern cameras.

I now turn to the task of bringing angular control to the wide field microscope. Figure 3.1 c) shows a configuration of the specimen with two in-focus beads (5) and (6), and one out-of-focus bead (7). The angular illumination control is ineffective for this arrangement of beads. If both in-focus beads, (5) and (6), are exposed simultaneously, i.e. an extended light source illuminates the entire field, then the out-of-focus bead (7) is always excited.

Only by separate illumination of the in-focus beads (8) and (9), as shown in Figure 3.1 d), angular control regains its function. For this reason a wide field system with angular control, using a mask in the pupil, requires an additional mask conjugate to the field. Therefore, we call our method spatio-angular microscopy.

3. The concept of spatio-angular microscopy

"Spatial" refers to the illumination control in the field and "angular" refers to the control in the pupil plane.

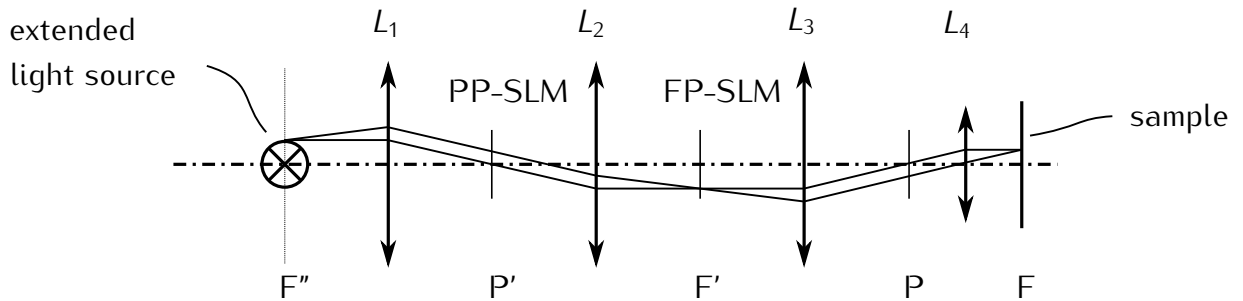


Figure 3.2.: Simplified schematic of the illumination system in our spatio-angular microscope. A homogeneous extended light source delivers light from the left. It is imaged by lenses L_1 and L_2 into the intermediate image F' . Then the tubelens L_3 and the objective L_4 form an image of F' in the sample plane F . We use two spatial light modulators (SLM) to control the spatial and angular light distribution in the specimen—the focal plane SLM in F' , and the pupil plane SLM in P' .

(fig:memi-simple)

Figure 3.2 shows the optical path through our prototype in a simplified form. From the left side, an extended light source illuminates the system. A sequence of telecentric lenses L_1 , L_2 , L_3 and the objective lens L_4 image the light source from F'' into the front focal plane (indicated by F , for field). The etendue (see page 26 for its definition) of the light source must be large enough to simultaneously fill both, the pupil P as well as the field F .

In each of the two planes P' and F' we place a spatial light modulator (SLM) that allows to control the intensity of the transmitted light.

Looking at the scheme in Figure 3.2, one might argue that we could save a lens, if we placed the pupil plane SLM into P instead of P' . There are three reasons why this is neither possible, nor beneficial: First, the pupil of modern high-performance objective lenses is typically not accessible. Second, the detection path for fluorescent light should contain as few optical components as possible and we can definitely not afford it to be blocked by a SLM. Third, the two masks induce non-linear, and therefore difficult to predict, filtering of spatial frequencies. An analysis requires consideration of partial spatial coherence, but it should be clear (FIXME) that only the downstream² SLM will always deliver a good image, mostly independent of the state of the SLM upstream.

Considering the fact that the image of the focal plane SLM is most important to us, we decided to place it downstream of the pupil plane SLM. The focal plane

²Downstream regarding the propagation direction of the excitation light.

3. The concept of spatio-angular microscopy

SLM may disturb the image of the pupil plane SLM in P, but we can always produce very fine, high-contrast structures in the sample F.

The ability to achieve high resolution in the field is the main difference between our approach and Levoys light field microscope. In the light field microscope, the density of the microlenses noticeably limits the resolution. As opposed to our system, the light field microscope allows to control the angle of incidence in all field positions independently. But, additionally to the reduced focal plane resolution, this requires a single high-resolution SLM with a comparatively low refresh rate. We use two small SLMs, which can each achieve 1 kHz frame rate and enable interesting experiments, e.g. optogenetic control of neuron activities.

Furthermore, structured illumination with high resolution patterns allows us to circumvent the missing cone problem of the widefield microscope. Later I will show that depth discrimination improves with higher resolution patterns (FIXME ref).

3.2. An imaging protocol with spatio-angular illumination control

3.2.1. Description of an exemplary biological specimen

I now refer to the *C. elegans* test sample for phototoxicity that I introduced in section 1.1. So far I did not reach the point of being able to image the development of a real embryo. Key problems are the low light throughput of the illumination system and the length of time necessary to update images on the focal plane display. Nevertheless, I always kept this example in mind while I was developing the control software for our microscope.

During the first few hours, the embryo develops confined within the constant volume of its egg, which has an ellipsoidal shape, extends 40 to 60 microns and can be readily observed using a 63× objective lens. Cell divisions occur every few minutes. During development the nuclei get smaller and more dense. In order to track the fate of all individual cells it is sufficient, to capture one stack per minute with 41 layers and a z-step of 1 micron.

3.2.2. Preparation of living embryo samples

For an experiment a hermaphrodite worm is cut and the embryos are placed on an agarose pad, so that they stay immobile during imaging. This procedure is

3. The concept of spatio-angular microscopy

explained³ in Hope (1999). Of these embryos, the experimenter chooses a young specimen, that has not yet divided. We avoid to use fluorescence excitation for this step. The undivided embryos can be distinguished using the less phototoxic differential interference contrast (DIC) imaging mode.

3.2.3. Sectioning through structured illumination

To get an estimate of the initial distribution of the fluorophores in the embryo I obtain the very first stack with structured illumination and no angular control. I use this method to avoid the missing cone problem of the widefield microscope. Perhaps for our particular task of finding the position of one nucleus within the egg, widefield images would be just sufficient. However, for our spatio-angular method, knowledge about the fluorophore distribution is very important and therefore we built our microscope such that we can obtain optical sections.

We compared conventional structured illumination using max–min (FIXME) reconstruction with laser and LED illumination. Although LED illumination resulted in excellent optical sections, the reconstruction of laser illuminated images contained artifacts.

Therefore, we decided to implement HiLo (see Appendix FIXME). With this algorithm, we obtain artifact-free optical sections, regardless of the illumination source. As another advantage the HiLo method increases acquisition speed, because only two raw images per slice are necessary.

3.2.4. Computer model for the integration of a priori knowledge about the biological events

Given an initial measurement of the fluorophore distribution of the embryo, I employ a computational algorithm to find good illumination conditions for subsequent stack acquisitions. An important requirement is that the computer can estimate, which areas of the sample should be protected from illumination.

For our test system, the *C. elegans* embryo, it is a promising approach to represent its three-dimensional fluorophore distribution by a simple model: Spheres encompassing the nuclei, indicate regions with fluorophores. When in focus, the spheres are the source of useful, informative fluorescence signal, but should be protected against exposure when out of focus.

³Note that Murray et al. (2006) describes an improvement of this protocol that prevents squeezing the embryos too much.

3. The concept of spatio-angular microscopy

As I mentioned earlier, there are also unused histones with fluorophores outside of the nuclei. The images reveal that they occur in the cytoplasm at a much lower concentration than in the nuclei. Fluorophores in the cytoplasm have a smaller phototoxic effect, because any radicals they produce are much less likely to reach the DNA and therefore inflict substantially less damage. In the following my goal is to protect only out-of-focus nuclei from exposure. The regions in between are used to bring the light in.

During observation, the nuclei, i.e. the centers of the spheres, move slowly within the embryo. For small periods of time we can describe this movement using a vector field of growth velocities.

A cell division announces itself by a change of the fluorophore distribution of the nucleus due to chromatin condensation and spindle formation. Therefore, whenever the computer detects such changes in the images, in one of the following time steps an additional sphere should be introduced to account for the new daughter cell.

So far I have implemented a simple algorithm, to convert a time series of image volumes from a confocal microscope into a sphere model (Santella et al. 2010). One of our project partners (Jean-Yves Tinevez, <http://fiji.sc/wiki/index.php/TrackMate>) developed a more sophisticated plug-in for ImageJ, that provides the lineage tree and snapshots of the developing cells (see Figure 3.3). Before our microscope can

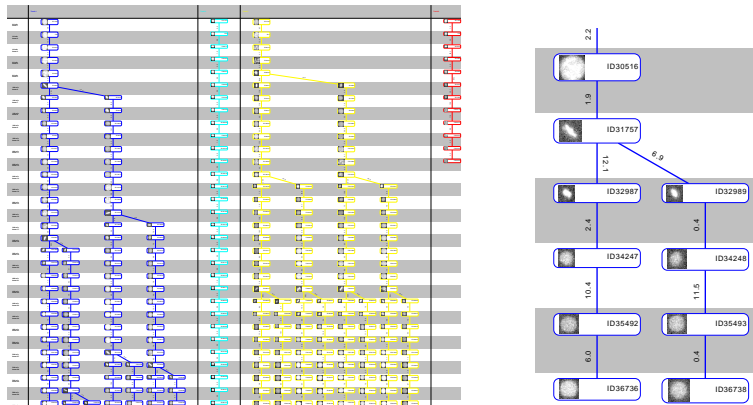


Figure 3.3.: A detail of a lineage tree visualized in TrackScheme. An image of each nucleus is shown in each time step. Note the elongated structure of the nucleus before the cell division event.

(fig:trackmate)

be used for our biological problem, the computer model has to be extended so that it reliably tracks the movement of nuclei. Overlooking any nucleus would prevent this nucleus from being imaged in later acquisitions and would be a setback for the experiment. Estimating the vector field of growth velocities helps to track

3. The concept of spatio-angular microscopy

nuclei more robustly and allows to predict their positions for the next exposure.

Currently we have not implemented programs that would fulfill the requirements for imaging a developing embryo. However, in the following text I assume that the described position predictions were available and I discuss how I determine masks for the focal plane and pupil plane SLM.

Murray et al. (2006)

TODO FIXME Bernhard Kauslers work is nice [http://archiv.ub.uni-heidelberg.de/v](http://archiv.ub.uni-heidelberg.de/volltexte/2011/3117/)

Live-cell microscopy image analysis for the study of zebrafish embryogenesis

http://hci.iwr.uni-heidelberg.de/publications/mip/techrep/kausler_12_discr

A Discrete Chain Graph Model for 3d+t Cell Tracking with High Mis detection

Robustness

(FIXME read this)

3.2.5. Illumination optimization by means of raytracing

I now discuss a method to find both SLM masks for image acquisitions with minimal phototoxicity. First I define a mask for the focal plane SLM:

From the predicted arrangement of spheres we select in-focus nuclei by intersecting the model with a planar surface. I then define focal plane SLM masks to selectively illuminate each of the in-focus nuclei, by drawing a bright disk in the appropriate position.

Based on such a mask, we can determine which angles can illuminate the in-focus target nucleus, without exposing out-of-focus nuclei.

As I already explained at the beginning of this chapter on page 39, ray-optical theory suffices to describe the light distribution within the sample.

I connect the periphery of an out-of-focus nucleus with a point inside the in-focus target. This defines a circular cone of rays, that are propagated through the objective lens. Their intersection with the pupil plane results in a figure that still very much resembles a circle—I found that already seven rays lead to good representation of its perimeter. An algorithm computes these figures for every out-of-focus nucleus and for a few in-focus targets points within the bright areas of the focal plane pattern. In this manner I construct the desired mask for the pupil plane SLM.

In order to trace the rays into the pupil, I need the design parameters of the objective lens (vertex position, curvature and material for all surfaces). Unfortunately, these rarely are publicly available for high-performance objective lenses. Nevertheless, in chapter (FIXME) I use a simpler model of the objective lens, that

3. The concept of spatio-angular microscopy

requires only three parameters: focal length, refractive index of the immersion medium and numerical aperture. These are always known.

Additionally, I have adapted the model for non-index-matched embedding of the specimen. This problem occurs when the embryo is illuminated with an oil immersion objective, using HILO (FIXME ref). It should be noted, however, that good image quality of the embryo can only be achieved with an objective lens that has the same immersion index as the embryo. Otherwise data from 20 microns within the sample will be severely deteriorated by spherical aberrations.

4. Description of our prototype for spatio-angular illumination

`{sec:dev1}` In the preceding chapter I showed the underlying concept of our spatio-angular microscope. Here I discuss additional details that are important for the practical implementation.

I explain the beam path, electronic synchronization of the displays with other components and an algorithm to transform the coordinate system of the camera pixels into the coordinate system of the focal plane SLM.

The pupil plane SLM was specifically developed for our project by our partner Fraunhofer IPMS (Dresden, DE).

4.1. Description of the optical components

So far I have only shown the beam path for transmissive displays (in Figure 3.2). Such SLM only have a very low transmission in practice. Therefore we use reflective displays in our prototype.

In Figure 4.1 I adjusted the beam path accordingly. This schematic also depicts the optics we use to adapt light from the laser to fill the etendue of our system. The light source enters the system from the bottom left. The optic components are color corrected and have anti-reflex coating for wavelengths in the range from 400 nm to 700 nm.

The system successively illuminates the pupil plane SLM — a grayscale micromirror array developed by our project partner Fraunhofer IPMS Dresden — and the focal plane SLM, a commercial binary liquid crystal on silicon display.

I gathered some of the following details from the documents that were created during the development of our prototype and are classified as confidential. I have summarized the key decisions here and the relevant project partners have agreed to the publication.

4. Description of our prototype for spatio-angular illumination

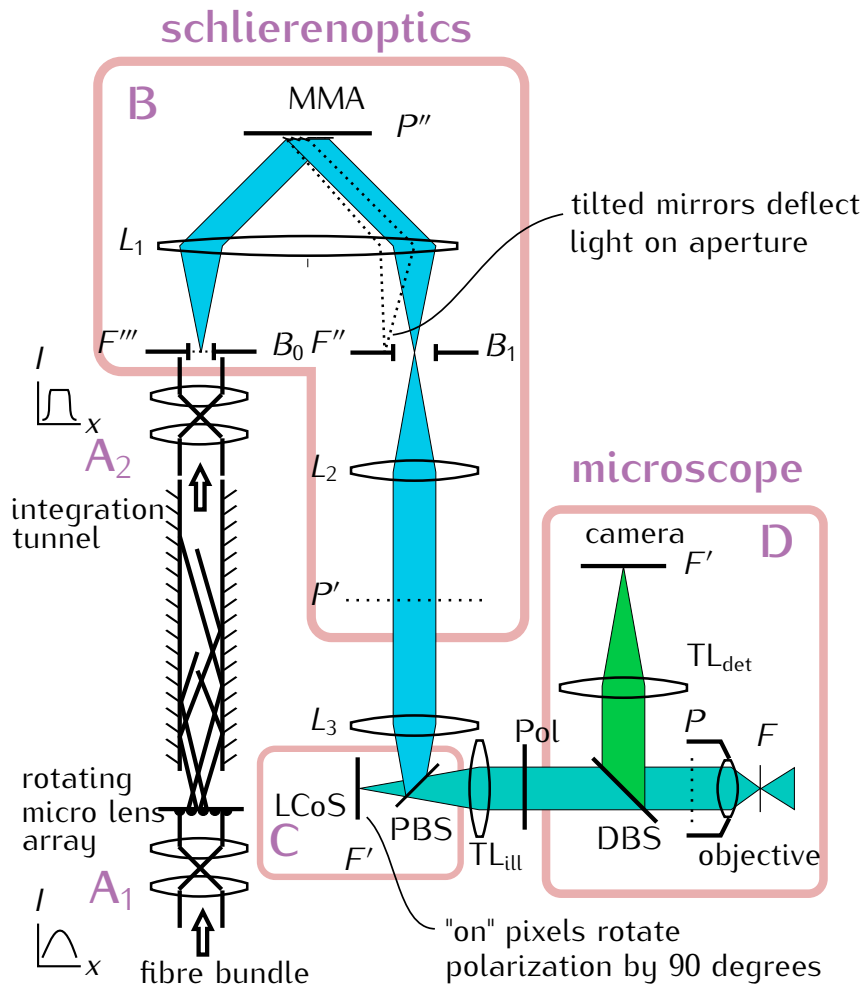


Figure 4.1.: Schematic of the light path through our microscope. Laser light enters from the lower left, is scrambled and homogenized to illuminate the pupil plane SLM in P'' and the focal plane SLM in F' . F is the field plane in the sample and its primed versions are conjugated planes. P is the pupil of the objective. Field mask B_0 and Fourier stop B_1 are adjustable circular apertures. PBS is a polarizing beam splitter. DBS is a dichroic beam splitter. The red boxes delineate subsystems of the illumination system: **A₁** and **A₂**: light scrambling and homogenization, **B**: Fourier-optical filter to provide intensity modulating pupil plane SLM. **C**: Polarization based intensity modulator as focal plane SLM. **D**: Wide-field fluorescence microscope with detection path.

(fig:memi-real)

4. Description of our prototype for spatio-angular illumination

4.1.1. Ensuring homogeneous illumination

A quantitative evaluation of our experiments (FIXME ref sec:results) with different illumination patterns is simplified when both pupil plane SLM and focal plane SLM are uniformly illuminated.

We use either a laser¹ or a light emitting diode (LED) as the light source in our experiments. Below we discuss optical measures that attain homogeneity of the illumination of both displays.

The LED² we use has a large active area. Due to etendue mismatch a relatively large amount of its produced light will never reach the sample. But it is easy to achieve a homogeneous illumination. Moreover, the LED can be quickly switched on and off electronically.

Unlike an LED, a laser delivers light of considerably higher spectral radiance ($\text{W}/(\text{sr m}^2\text{m})$). Thus it is in principle possible to use the laser as a highly efficient light source for our system. Unfortunately, the high spectral and spatial coherence of a laser often lead to high-contrast fluctuations of the irradiance and we have to compensate for this by time averaging.

When using the Laser, we send its parallel Gaussian beam into a bundle³ of randomly distributed fibers. This randomizes the light distribution at the bundle output and also broadens the illumination angles.

A relay system (A_1) images the circular output of the fiber bundle onto the entrance of a light pipe. This relay system contains a rotating microlens array⁴. It is driven by a motor with the axis of rotation being displaced from the optical axis. This time-varying element allows to reduce speckle.

Both, the fiber bundle and microlens array, increase the etendue of the laser illumination to the optimum value, which is given by one of our SLM as discussed on page 54.

The light pipe is a hollow mirror-integrator tunnel with quadratic cross-section and depicted in Figure 4.2. The mixing effect of the tunnel can be understood by considering the irradiance in the plane of the tunnel output as it would occur without tunnel.

Drawing the outline of the square cross-section into this irradiance map selects the light that directly reaches this plane. Surrounding this outline with four

¹Lasever LSR473H, diode-pumped solid state laser, output power 600mW, $\lambda = 473 \text{ nm}$

²Huey Jann HPB8-48KBD, wavelength $(463 \pm 1) \text{ nm}$, brightness 35lm, view angle 120°

³Fiber bundle with circular cross-section (Loptek, Berlin, DE), 1.1 mm diameter and 2 m length.
The beam broadening is 3° and increases, when the bundle is bent (Ipp et al. 2009a).

⁴Array of cross-oriented cylindrical lenses on both sides with a pitch of 0.5 mm resulting in an effective focal length of 6.9 mm (LIMO, Dortmund, DE).

4. Description of our prototype for spatio-angular illumination

identical copies that touch its edges selects the light that will reach the output plane after one reflection. The irradiance maps from neighbouring squares are mirrored and added to the direct illumination. Depending on the numerical aperture of the input light, more reflections may occur — resulting in the addition of irradiance from next-nearest-neighbours and so forth.

This improves the uniformity of the light distribution in the output plane without altering the numerical aperture of the light. The more subregions are superimposed, the better will be the uniformity. Assuming N subregions were overlaid and their contributions were statistically independent, then according to the central limit theorem the standard deviation of the irradiance is proportional to $1/\sqrt{N}$ (Koshel 2012).

However, we also align the source distribution to be rotationally symmetric about the optical axis and obtain an even more uniform output than what would follow from this prediction because positive and negative slopes from different subregions compensate in the superposition (also Koshel (2012)).

In our system the side length of the cross-section of the tunnel is 2.5 mm and its length of 250 mm ensures enough reflections for homogeneous illumination. A relay system magnifies the tunnel output to $4\text{ mm} \times 4\text{ mm}$ in the plane F'' .

We thought about using the output of the tunnel directly, without the additional relais system, but then the length of the tunnel would have been prohibitively long.

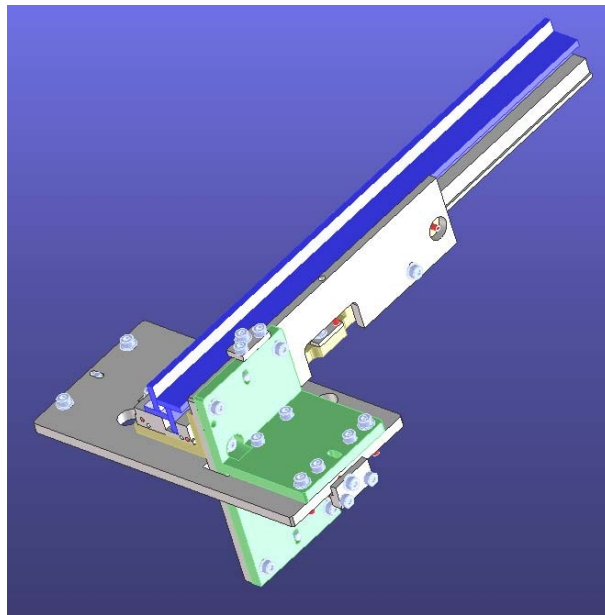


Figure 4.2.: Hollow mirror-integrator tunnel with a quadratic cross section of 2.5 mm side length and 250 mm length.

(fig:integrator-rod)

4. Description of our prototype for spatio-angular illumination

Regarding the two relay systems the optical designer at In-Vision commented (Ipp et al. 2009b) that these have not been optimized for perfect imaging but for the transport of the homogeneous light distribution. The system A_1 at the tunnel entrance has to transfer the illumination from the round fiber end to the square tunnel entrance. The engineer designed a good quality system with only two lenses (and the microlens array). At the other end (A_2 in Figure 4.1) five elements carry the light from the tunnel exit into the field mask B_0 in F'' .

During the planning phase we also considered a homogenization design based on a fly's eye condensor (two consecutive microlens arrays). According to simulations performed by In-Vision, this, however, would have been more difficult to adjust than the tunnel. In particular the system would have been more dependent on illumination wavelength.

In summary the following points are important in order to achieve homogeneous illumination of focal and pupil plane with the tunnel:

- The image of the end of the bundle should properly cover the tunnel entrance. Especially the corners of the tunnel should not be darker than the center. Inhomogeneous illumination at the tunnel entrance leads to inhomogeneous illumination of the pupil plane SLM.
- The end of the fibre bundle must be adjusted in four axes (centering and angle).
- The focal length of the microlenses should be chosen shorter than predicted by pure etendue calculation. In order to compensate inevitably occurring microchipping on the edges of the cemented glass mirrors.

4.1.2. Fourier optical filter for contrast generation on pupil plane SLM

The micromirror array, which we use as a pupil plane SLM consists of torsion mirrors that modulate

FIXME translate

besteht aus Torsionsspiegeln. Aktuatordesign (Schmidt et al. 2010) Grauwerte, Kontrastmessung (Berndt et al. 2010) Kalibrierung (Berndt et al. 2011; Berndt 2007)

the phase of the light (see Figure 4.3 for images of the device). In order to modulate the intensity we use the Fourier optical filter denoted as 'schlierenoptics' in Figure 4.1 B.

4. Description of our prototype for spatio-angular illumination

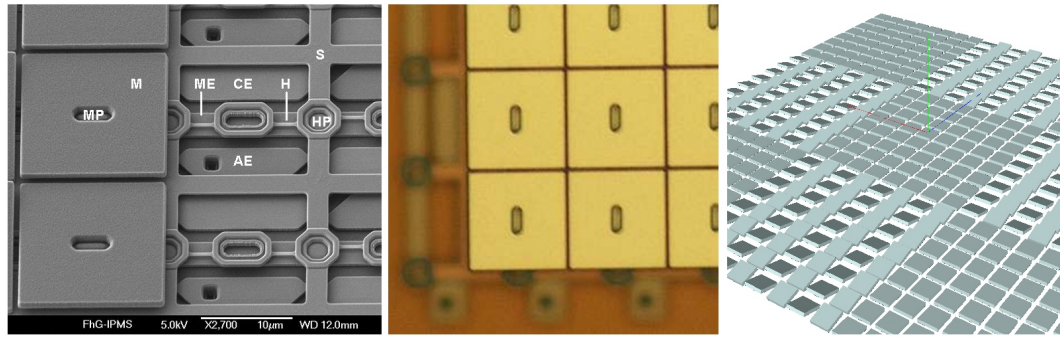


Figure 4.3.: **left:** Scanning electron microscope image of the micro-mirror array (MMA). The pixel pitch of the device is 0.016 mm. The hinges for the tilt movement and the electrodes are clearly visible. **middle:** Optical reflective microscope image of the MMA. **right:** exaggerated rendering of how a 8x8 checker board pattern would be displayed on the device. Electron and optical micrograph by Fraunhofer IPMS Dresden (Germany)

(fig:mmma)

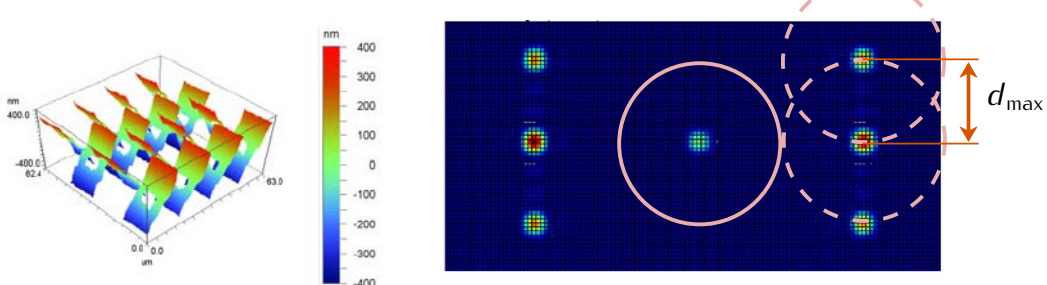


Figure 4.4.: **left:** Measurement of the deflection of micro-mirrors using a white-light interferometer (provided by Fraunhofer IPMS Dresden (Germany)). **right:** Simulation of the Fraunhofer diffraction pattern of the micro-mirror array for coherent, monochromatic light (kindly provided by Joel Seligson). The circles with radius d_{\max} indicate the maximum size of the field mask B0 where the diffraction orders do not overlap. This limits the etendue of our illumination system.

(fig:mmma-fft)

The lens L1 has two purposes: First, it images the field mask B0 into the Fourier stop B1. Second, the plane P'' with the phase SLM is imaged to infinity.

With undeflected micromirrors, the SLM has no significant effect and works like a plane mirror. Both planes F'' and P' are then homogeneously illuminated.

If the left half of the micromirrors are tilted, then they direct the light along the dashed line in Figure 4.1. This light is absorbed by the field stop B1 and therefore missing in P', i.e. the right side in P' is dark. The total radiant flux (W) through the beam stop in F'' decreases while the transmitted irradiance (W/m^2) remains

4. Description of our prototype for spatio-angular illumination

homogeneous. In the real system, the lens L1 consists of four glass elements.

Fourier diffraction pattern

The phase distribution $\Phi(x)$ in MMA plane corresponds to the profile in Figure 4.4 left:

$$\Phi(x) = \sum_p \left[\underbrace{\left(\exp(i\mathbf{k}(p_x, p_y)x) \cdot \text{rect}(x, y) \right)}_{\Phi_p} \otimes \delta(x - p_x\Delta x, y - p_y\Delta y) \right] \quad (4.1) \quad \text{eq:mmma-com}$$

where $x = (x, y)$ is a position in the MMA plane, the rectangular function rect delimits an individual micro-mirror with its deflection encoded in $\mathbf{k} = (k_x, k_y)^T$. The index vector $p = (p_x, p_y)^T$ indicates the mirror position.

The diffraction pattern of an individual mirror is a sinc-function which is shifted according to the mirror deflection and a phase gradient which depends on the mirror position p :

$$\tilde{\Phi}_p(\mathbf{k}) = \mathcal{F}(\Phi_p(x)) = \text{sinc}(k_x - k(p_x, p_y)) \cdot \exp(i\mathbf{k}(p_x\Delta x, p_y\Delta y)) \quad (4.2)$$

Adjacent rows of mirrors tilt in opposite directions ($\pm x$). Therefore, we can specify the term $\Phi_p(x)$ in equation 4.1 more precisely and obtain two expressions:

$$\Phi_p^{(1)}(x, y) = e^{+ik_0x} \text{rect}(x) \otimes \sum_p \delta(x - p\Delta x) \quad (4.3)$$

$$\Phi_p^{(2)}(x, y) = e^{-ik_0x} \text{rect}(x) \otimes \sum_p \delta(x - p\Delta x) \quad (4.4)$$

A good analytical description of the surface of the MMA is:

$$\begin{aligned} \Phi(x) &= \Phi_p^{(1)}(x, y) \left(\text{rect}(y) \otimes \sum (\text{every second row}) \right) \\ &\quad + \Phi_p^{(2)}(x, y) \left(\text{rect}(y) \otimes \sum (\text{every second row, shifted by one}) \right) \end{aligned} \quad (4.5)$$

Figure 4.4 right shows a numerically calculated diffraction pattern of this structure for a monochromatic plane wave. Suppose the Fourier stop B1 blocks light outside of the circle with the solid line. Then the transmitted zero-order irradiance is proportional to the sinc^2 of the deflection angle. This applies more or less even if not all mirrors of the array are deflected. Therefore, we can modulate the irradiance in the plane P' using this optical system albeit the transfer function is non-linear.

An accurate prediction of the irradiance in P' is even more difficult to describe when the field mask B0 is opened and the extended source produces illumination

4. Description of our prototype for spatio-angular illumination

that is spatially partially coherent (?).

maximal etendue

But one thing is clear: The contrast can only achieve good results as long as higher diffraction (dashed circles in Figure 4.4 right) orders can not pass the Fourier stop B1. This limits the size of the field mask B0 to the diameter d_{\max} , assuming that no high frequency pattern is displayed on the MMA.

The smallest distance between the orders in Figure 4.4 right corresponds to a structure size Λ of two mirror pitches: $\Lambda = 32 \mu\text{m}$. Therefore the diffraction angle θ is:

$$\sin \theta = \lambda / \Lambda \quad (4.6)$$

Utilizing this, we can express the maximum radius:

$$d_{\max} = f_{L1} \tan \theta \approx \frac{f \lambda}{\Lambda} \quad (4.7)$$

Here, f_{L1} is the focal length of lens L1. With the F-number $\# = f_{L1}/(2d_{\max})$ we can find the maximum etendue of the Fourier optical system:

$$\mathcal{E} = \frac{\pi A}{4\#^2} = \frac{\pi A \lambda^2}{\Lambda^2}, \quad (4.8)$$

with the area $A = (4 \text{ mm})^2$ of the micro-mirror array.

For our system the maximal etendue is between $0.0079 \text{ mm}^2/\text{sr}$ and $0.024 \text{ mm}^2/\text{sr}$, depending on the wavelength. This is much smaller than the etendue of a typical microscope objective ($0.27 \text{ mm}^2/\text{sr}$, see section 1.3.3) and corresponds to a field diameter D_{field} in the specimen between $70 \mu\text{m}$ for a wavelength λ of 400 nm and $125 \mu\text{m}$ for 700 nm , with

$$D_{\text{field}} = \frac{2}{\text{NA}} \sqrt{\frac{\mathcal{E}}{\pi}}, \quad (4.9)$$

where NA is the numerical aperture.

4.1.3. Relay optics between pupil plane and focal plane SLM

The lenses L2 and L3 form a double-telecentric relay system with magnification 2 and image F'' onto the focal plane SLM in F' . At the same time these lenses make sure that the pupil plane SLM is imaged to infinity.

The relay system ensures that the pixels of the focal plane SLM are at the resolution limit, while the pupil plane SLM fills the pupil.

4. Description of our prototype for spatio-angular illumination

In addition, the relay system enables a simpler mechanical realization and good contrast. It would already be difficult to accommodate the focal plane SLM and polarization beam splitter in F'' — including an adjustable aperture would probably not be feasible at all.

4.1.4. Contrast generation on focal plane SLM using polarization

Why fLCoS and not DMD?

The SLM we use to control the focal plane illumination is a ferroelectric liquid crystal on silicon device (fLCoS, ForthDD WXGA R3, UK). Depending on if a pixel is off or on, the returning light either retains the polarization of the input light or rotates it by 90 degrees (Martínez-García et al. 2009). From this, a polarization beam splitter generates a binary intensity contrast (see Figure 4.1 C).

We have not opted for a digital micro-mirror device (DMD), because those mirrors have sharp edges and loose significant amounts of light into higher orders that can not contribute to the image in the specimen. The pixels borders of a fLCoS device are defined by electric fields and are therefore more blurred. At least in this sense, an fLCoS based device should be more efficient than a DMD.

We use a wire-grid polarization beam splitter (Moxtek PBF02C, Orem, UT, US) because they ensure a high enough optical quality, good contrast and the plate causes less back reflections than a beam splitter cube.

The s-polarized component of the incoming light is reflected towards the SLM. Active pixels of the SLM rotate the polarization of light by 90 degrees and then passes through the beam splitter as p-polarization in the direction of the microscope. There is a supplementary cleanup analyzer in the beam path.

It would also be conceivable to arrange SLM and beam splitter differently, so that the light coming from the SLM is *reflected* towards microscope. In this case, however, unwanted bending of the beam splitter's surface will deteriorate the image quality of the focal plane SLM. Therefore, we use the beam splitter in transmission.

The beam splitter plate makes the overall optics slightly asymmetric and thus induces mainly astigmatism and lateral color (Ipp et al. 2009b). The plate is thin enough (thickness 0.7 mm), so that the design remains diffraction limited.

4.1.5. Variable telescope as tube lens

Microscope objectives come with various pupil diameters. The last lens TL_{ill} in our illumination system has been designed as a variable zoom objective (by In-Vision,

polarizing beam splitter

4. Description of our prototype for spatio-angular illumination

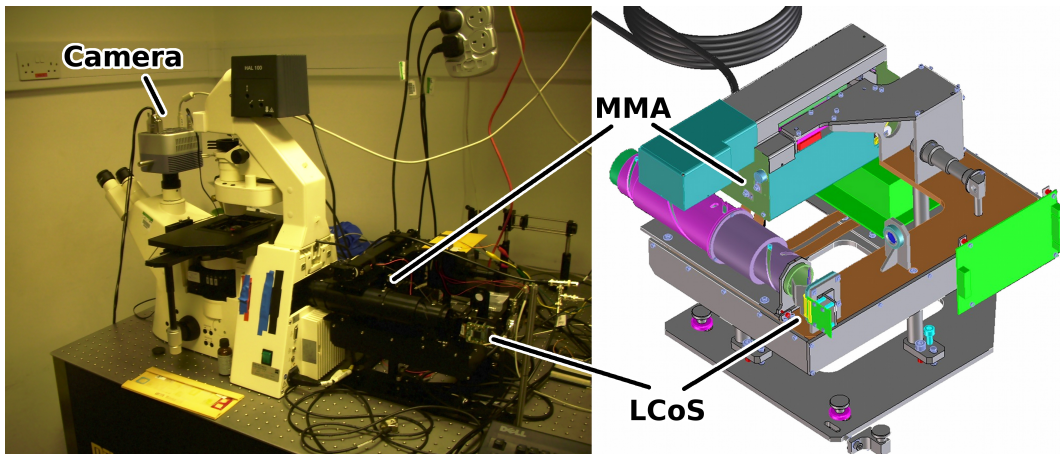


Figure 4.5.: The wide field epi-fluorescence microscope with attached illumination head. The positions of the two spatial light modulators (pupil plane SLM: micromirror array (MMA) and focal plane SLM: liquid crystal on silicon display (LCoS)) are indicated. Drawing by Josef Wenisch (In-Vision, Austria).

tup-photo-blueprint)?

Guntramsdorf, Austria), that maps the pupil plane SLM from P'' with variable magnification to P .

Unlike conventional zoom telescopes we use three movable lens groups to guarantee that the image of the pupil plane SLM remains stationary while the focal plane SLM is always imaged into infinity during magnification changes.

4.2. Electronic control of the component

local pattern storage

Both spatial light modulators can run at most with 50% duty cycle. Therefore it is necessary to synchronize the displays. Their controllers allow to upload several hundred frames of image data at the beginning of an experiment and keep them in local storage. Images can then be selected by fast function calls over USB (focal plane SLM, fLCoS) or Ethernet (pupil plane SLM, MMA).

camera is master

The camera (Clara, Andor PLC, Belfast, Northern Ireland) as the slowest device is chosen as the master. It provides two TTL outputs. The output "fire" is high while the camera is integrating. The output "shutter" goes high 1 ms before "fire" and provides enough time ($> 850 \mu\text{s}$) for the MMA controller to tilt and let the mirrors settle.

The LCoS controller can display its images only for certain discrete times (20 ms, 10 ms, 5 ms, 200 μs) and it is not straight forward to change this via USB interface. Therefore we always work with a fixed LCoS display time of 20 ms. The "fire"

4. Description of our prototype for spatio-angular illumination

output of the camera also switches the laser on using an acousto-optic modulator (AOM).

When the z-stage is used, the camera is stopped until the stage has reached its target position.

5. Experimental results with spatio-angular microscope

?<sec:results>

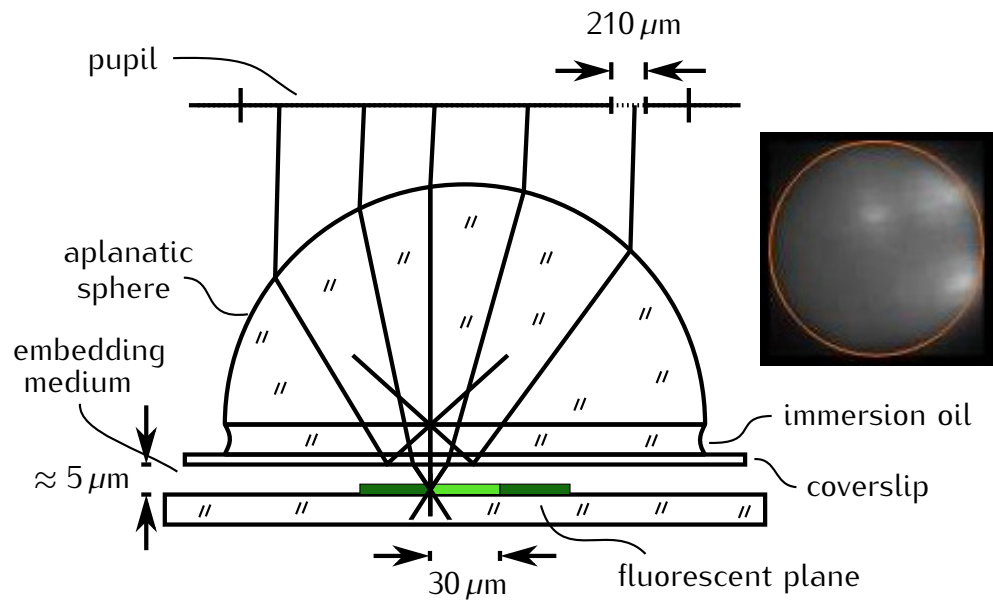


Figure 5.1.: A fluorescent plane on a slide is embedded in oil, water or air. The thickness of the embedding medium is approximately $5 \mu\text{m}$. The focal plane SLM illuminates a disk with $30 \mu\text{m}$ diameter while a 15×15 window is scanned over the MMA. The window corresponds to a square with $210 \mu\text{m}$ on the side as opposed to 3.6 mm BFP diameter
right top: Typical camera image, the orange circle indicates the $30 \mu\text{m}$ illuminated area. camera image.

?<fig:tirf-exp>

5. Experimental results with spatio-angular microscope

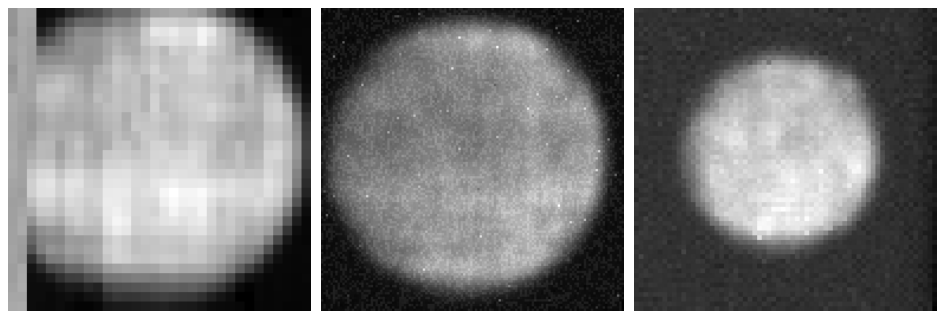


Figure 5.2.: Integrated image intensities for different illumination window positions in the back focal plane. Embedding media: **left:** Oil $n = 1.52$, **middle:** water $n = 1.33$, **right:** air $n = 1$.

:immersion-bfp-scan)?

gel with fluorophore Rückerl et al. (2013)

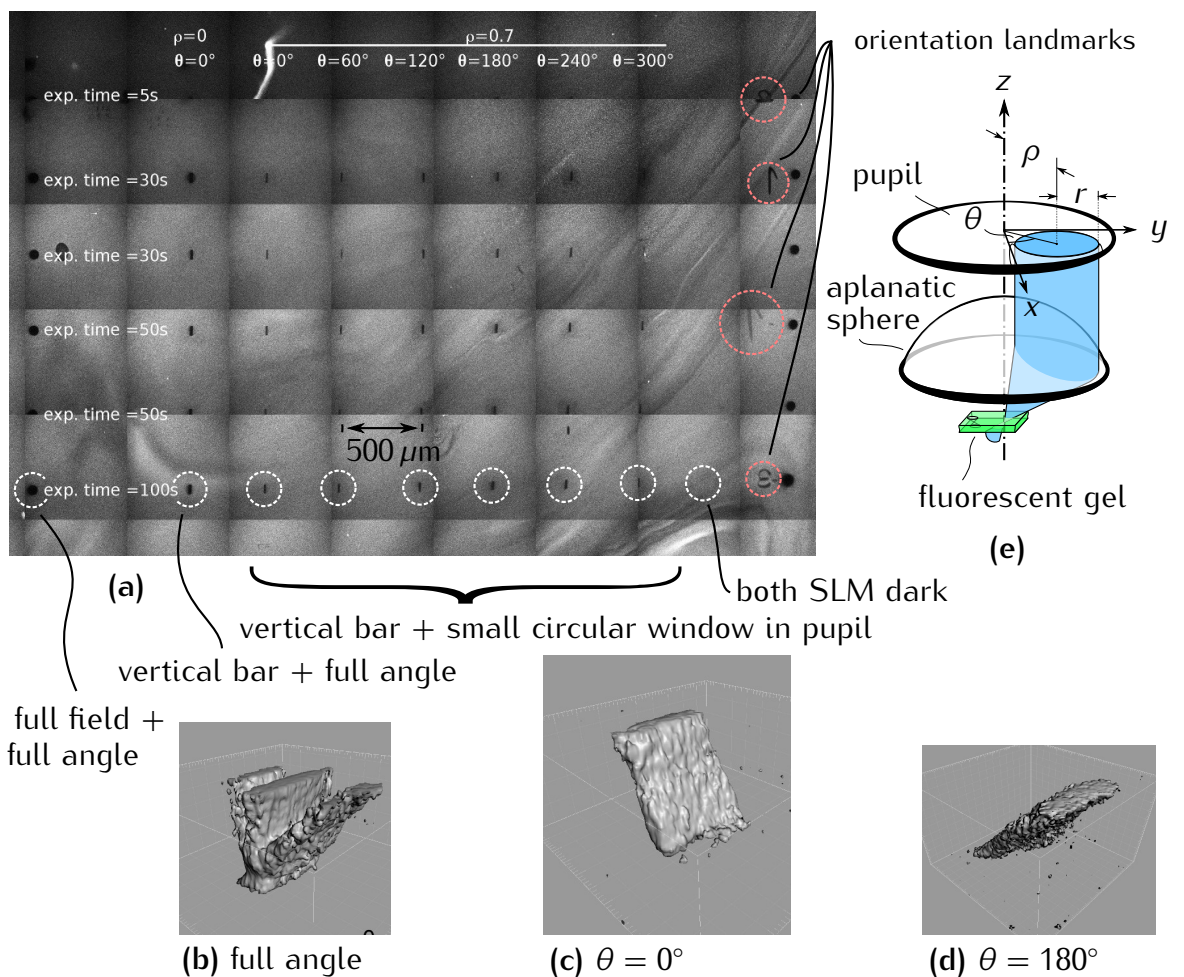


Figure 5.3.:

fig:overview-bleach)?

5. Experimental results with spatio-angular microscope

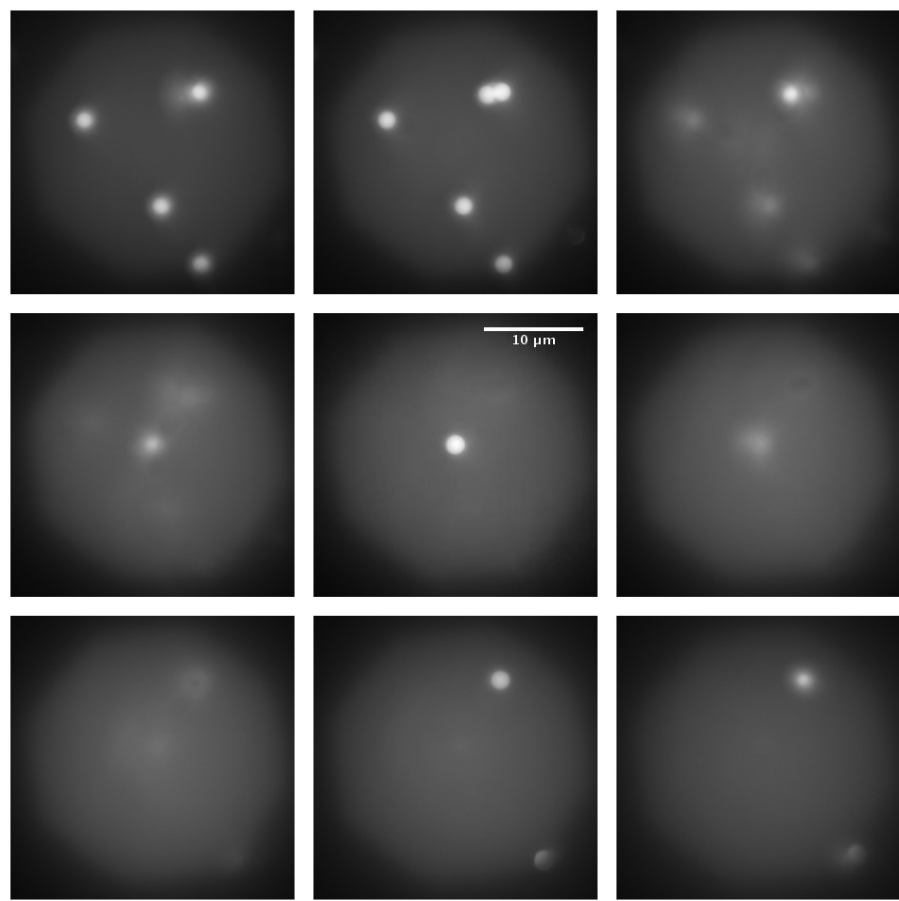


Figure 5.4.: Wide field stack of a three-dimensional distribution of yellow-green beads in agar. Sampling in z is $1 \mu\text{m}$.

`{fig:m_wf}`

5. Experimental results with spatio-angular microscope

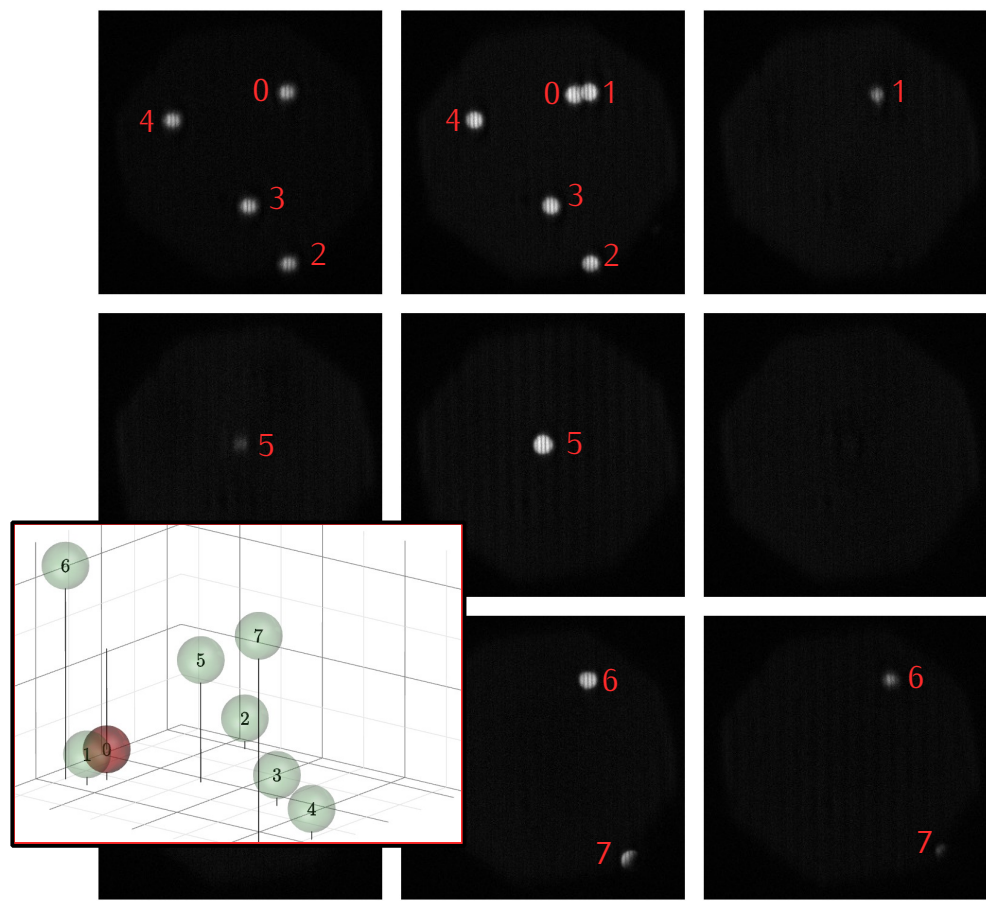


Figure 5.5.: Computationally sectioned images. Note that two beads (4 and 7) are very close to the border of the field of view and not fully illuminated.

{fig:m_sec}

5. Experimental results with spatio-angular microscope

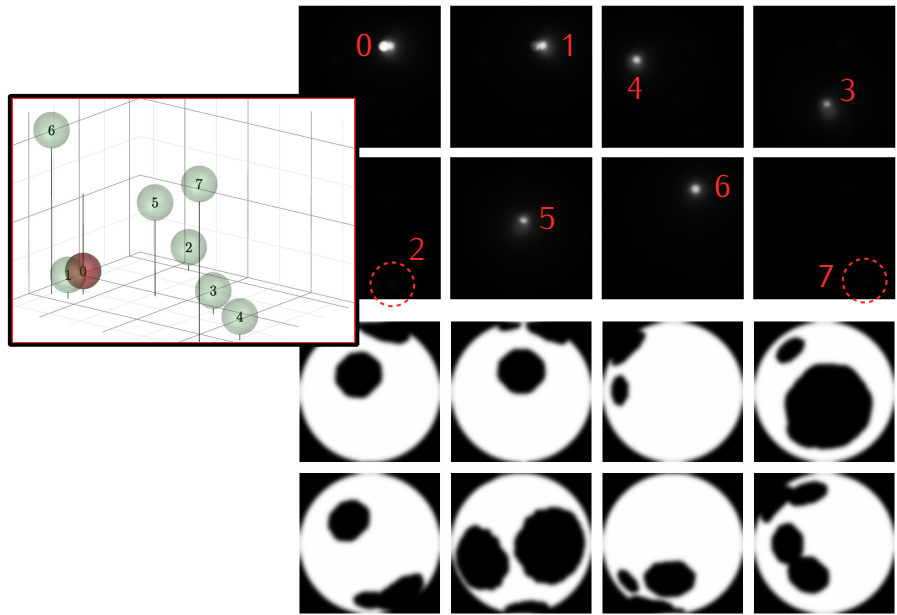


Figure 5.6.: Spatio-angular controlled illumination of the beads from Figure 5.5.
The top left image shows bead number zero and so forth, the second image in the top shows bead number one and so on. The LCoS selectively illuminates the target bead and the MMA displays the pattern shown in Figure ??.

?(fig:m_ang)?

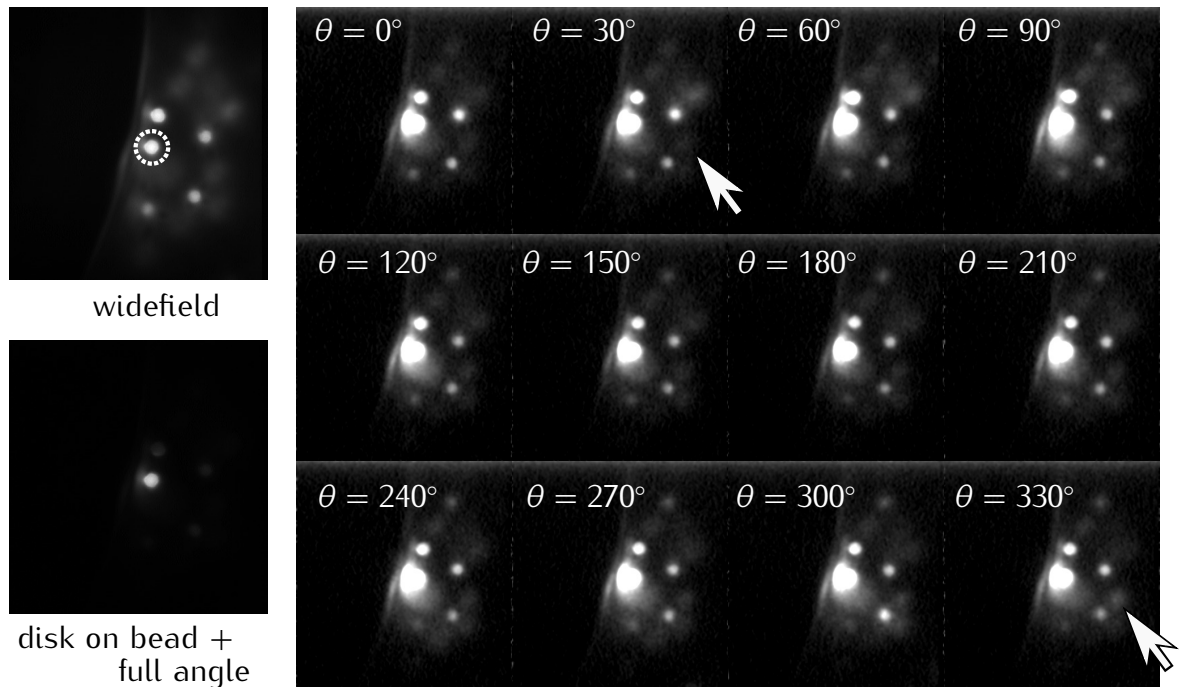


Figure 5.7.:

?(fig:montage-ang)?

6. Discussion

?<sec:discussion>

This thesis deals with the practical development of a wide-field fluorescence microscope system that can control the irradiance in the specimen as well as the illumination angles with the aim of decreasing phototoxicity.

origin of the idea

The original idea was to combine a programmable array microscope with a control of the illumination directions. Initially this seems to be an elegant approach: The programmable array microscope produces two images on a camera, one of which contains only out-of-focus light. By variation of the illumination angle of the excitation light, it should be possible to find the direction with minimal out-of-focus contributions.

Fairly quickly it became clear that this approach, if at all, would work only inefficiently. After all, for the programmable array microscope to work, fine structures must be imaged into the specimen. This, however, has the consequence that several diffraction orders instead of one bundle of rays with similar directions must traverse the sample. For most specimens this will bring no advantage compared to a wide-field microscope.

We opted instead for a modification of the excitation path in a wide-field microscope. My assumption was that given an estimate of the 'to-be-imaged' three-dimensional fluorophore distribution, and perhaps additional information on the expected movement of cells, pathogens or organs; a sufficiently accurate prediction of the expected out-of-focus light can be made.

description of the hardware

Using two spatial light modulators (SLM), we can project appropriate distributions of excitation light into the sample. One SLM controls the angle and the other the in-focus pattern of light. Our goal for the instrument was that it can capture one stack per minute, consisting of twenty slices. For this, partial recordings of slices should be acquired in sequence and later composed into one image. Therefore We selected the SLM devices with an emphasis on high speed.

The fastest commercially available SLM are ferroelectric liquid crystal on silicon devices (fLCoS) and digital micro-mirror devices (DMD), which both can only do binary modulation. However, in our case binary intensity modulation is disadvantageous. Sharp edges lead to high diffraction losses and strong

6. Discussion

oscillations of the field in the Fraunhofer diffraction pattern.

The pupil plane SLM, that controls the illumination angles does not necessarily need a high resolution but a binary SLM device should be avoided here because otherwise oscillations of excitation intensity would occur in the specimen and appear on the camera image. For this reason, we use a specifically developed SLM, which resembles a DMD in terms of mode of operation and speed but can display gray scale values.

The focal plane SLM, on the other hand, should have a high resolution and it should be possible to update its patterns very fast, depending on recent camera acquisitions. Initially I opted for a SLM that is connected to the graphics card of a computer. We chose a fLCoS SLM because its pixel borders are less sharp than the DMD and we expected a better efficiency for our application. Unfortunately there were difficulties with the synchronization of the graphics card and the other devices. Therefore, relatively late into the project I had to replace the SLM controller with another one that contains internal memory and is linked to a computer via USB. Unfortunately, the USB connection is very slow and fast update of image patterns is no longer possible. In retrospect, it would have been easier to use two identical gray value SLM from Fraunhofer. Note that Institut Pasteur and Fraunhofer IPMS continue this work and do just that under the Joint-Programme Inter Carnot Fraunhofer PICF 2011, "Micromirror Enhanced Microscopic Imaging for high-speed angular and spatial light control in spectral Optogenetics and Photomanipulation applications in biological applications" (MEMI-OP).

A serious disadvantage of the Fraunhofer SLM in combination with the Fourier optical filter approach employed in our prototype is the small acceptance angle. This limits the exposed field to $80\text{ }\mu\text{m}$ diameter for a wavelength of 473 nm using a $63\times$ objective with a numerical aperture of 1.4, while the objective does support $400\text{ }\mu\text{m}$ field diameter. One solution could be contrast generation in a common path interferometer as described in the patent application (Heintzmann and Wicker 2010). The approach is derived from reflective Nomarski differential interference contrast microscopy. A birefringent prism separates the illumination bundle into bundles that have a small offset (shear). If the shear distance corresponds to the pixel pitch $\Lambda = 16\text{ }\mu\text{m}$ of the micro-mirrors then this device converts height differences between adjacent mirrors into intensity contrast. My experiments with a set of Nomarski prisms that were available in our lab gave an indication, that this method can work. However the prisms had too small a shear angle and returning diffraction orders were cut off. At this point in time, the planning for the original prototype was already so far advanced that a change was not possible.

Why Fraunhofer
micro-mirror array?

choice for focal
plane SLM

remedy against low
acceptance angle

6. Discussion

However, this is still a very promising method and will probably produce good results when prisms with larger shear angles are used. Additionally it should be noted that this method will work better for piston-type micro-mirrors than for torsion micro-mirrors.

priority of the control algorithm

Given the *low transmission* of our prototype, which could be just barely enough to investigate the biological test system of *C. elegans* embryos, the disproportionately high effort that went into synchronizing the two fast SLM which can only run at a *reduced duty cycle*, and the *limited etendue* which excludes some interesting experiments, it would have been better in hindsight, to build a demonstrator with two slow, conventional, gray-value SLM and to spend more effort on the development of the illumination control algorithm.

holographic system

In this context, with the aim of simplifying the hardware, I built a holographic illumination system consisting of a single phase-only SLM in the intermediate image plane. This enables simultaneous control of both, the in-focus light distribution as well as the illumination angles in the specimen. The SLM displays diffraction gratings and its arrangement is such, that the first diffraction order illuminates the pupil. The illumination angle in the specimen can be adjusted by the grating period and direction while the local irradiance is controlled with the grating contrast.

Unfortunately the phase-only SLM that I used for the experiments suffers from cross-talk between pixels, a non-linear transfer function and temporal fluctuations of the displayed phase pattern. It was uncertain whether these problems could be circumvented. Especially higher orders which are generated by the device's non-linearity and that can reach the sample are a problem, and it seems particularly difficult to project a finely structured grid into the sample. Projecting such patterns is necessary, because for my illumination algorithm I need a reasonably good measurement of the three-dimensional fluorophore distribution. For many specimen structured illumination is necessary to remove out-of-focus light from the raw images and obtain optical sections. Phase SLM which became available more recently have a much better performance and could probably be used to construct a holographic spatio-angular illumination device.

sectioning by structured illumination

Our prototype with two SLM is more suitable for structured illumination. The period on the focal plane SLM and the illumination aperture defined by the pupil plane SLM can be selected for best possible contrast of the in-focus light pattern. Optically sectioned images can be calculated with the usual methods. The HiLo method proposed by Jerome Mertz and best documented in Mertz and Kim (2010) is preferable to others as only two exposures per slice are necessary. Since

6. Discussion

images in our system are taken in rapid succession and movement artifacts are unlikely, we developed a variant of the HiLo method and in contrast to the original, which uses one uniformly illuminated image and one with structured illumination, we use two structured illumination images which gives better signal-to-noise.

sCMOS -- new camera technology

During my work on the project a much improved camera technology came to market. No such camera was used for measurements in this work, however, such a camera could be added to our system without substantial changes.

Arduino for control electronics

This change is made possible mostly due to the flexibility that the Arduino gives. This cheap and easy to use electronics platform has been used for several years in our lab and is particularly useful for synchronization of multiple devices. The source code for the Arduino microcontroller is often short and relatively easy to read. This controller is thus well suited to document the logic in our synchronization circuits and can be easily understood and extended by new members of our group.

During this work, I used many different electronic devices (SLM: Hamamatsu, Holoeye, ForthDD, Texas Instruments, Fraunhofer, cameras: Andor (Clara, IXon2, IXon3, IXon Ultra, Neo sCMOS), Photometrics Cascade II, Hamamatsu (Orca Flash 2.8 and 4.0), Logitech Pro 9000, and more). I noticed that construction and debugging effort depend very much on the quality of the documentation. If documentation is insufficient, which unfortunately is often the case, then it helps if communication is done with open standards (USB video device class, Ethernet).

Particularly positive I was surprised by the Texas Instruments DMD. The SLM development kit is very mature, contains open source software and high quality documentation explaining even the control registers of individual chips. While working with the kit I was able to implement features within three days, for which I spent several months of reverse engineering and trial and error on devices of other manufacturers. If I had known that before, I would have designed the prototype differently and I would have accepted some drawback regarding optical performance.

Open hardware is a good thing

I am particular unhappy with the state of scientific cameras as all of them gave me problems with incompatible or unstable drivers. Therefore, I hope that there will be more projects that open their resources to the public, such as Marc Levoy's Franken Camera (Adams et al. 2010); or that the manufacturers of the ever-improving consumer cameras document and disclose the protocols for disabling automatic image processing and accessing raw sensor data for their devices (as with the Logitech Pro 9000).

results of existing control software

Our prototype and the software for illumination optimization has been designed

6. Discussion

for the observation of cells in a developing *C. elegans* embryo. So far I was able to demonstrate spatio-angular illumination on static, non-living samples. So far I have not applied the method for living organisms. Here, the main problem is that image upload, especially to the focal plane SLM takes disproportionately long.

6.1. Outlook

proposal of an optogenetics experiment

If the sample does not change very fast, and plenty of time is available to upload images into the SLM controllers, then the current prototype allows experiments with rapidly changing illumination patterns (about 1000 fps should be possible). One interesting biological experiment would be similar to Branco et al. (2010). There, synapses were excited by moving a focal spot along one linear dendrite and its response was recorded as a function of the speed of the focal spot. With our system, two branches of a dendrite could be stimulated simultaneously and the response of the junction could be investigated.

next steps for control software

The algorithm for the optimization of the illumination patterns can still be improved. So far, I assume that the sample can be represented well by spheres. The nuclei in each slice are illuminated individually and the algorithm finds illumination angles so that exposure of out-of-focus nuclei is avoided. An obvious improvement would be to find nuclei that can be illuminated with similar angles and group them for simultaneous exposure. Even better would be an algorithm that does not need to represent the specimen as solid bodies but works directly on stacks of optical sections. In a first simple experiment, using the graphics processing unit, I could show that the extensive calculations can be carried out in reasonable time frames.

partial coherent simulation

Our work also leaves an unanswered question regarding the optics. It would be interesting to simulate the wave-optical image formation of the prototype with partial coherence. This would answer the question how important the gray levels of the micro-mirror array in the pupil-plane really are, and whether or not we can replace it with a binary DMD.

A similar simulation should be used to investigate the influence of field mask B0 and Fourier stop B1 on the contrast and the transfer function of the schlierenoptics system.

A. EM-CCD camera calibration

A.1. Andor Basic code listing for automatic image acquisition

```
ec:basic-acquisition)
    ' This is code for the Basic interpreter in Andor Solis
    function ~GetSaturatingExposure()
        SetKineticNumber(1)
        exp=.01
        SetExposureTime(exp)
        run()
        m=maximum(#0,1,512)
        GetSaturatingExposure=exp*10000/(m-100)
        CloseWindow(#0)
    return
    name$ = "C:\Users\work\Desktop\martin\20111111\scan-em3\xion_"
    print("start")

    SetOutputAmp(1)
    print("conv_start")
    exp= ~GetSaturatingExposure()
    print(exp)
    SetExposureTime(exp)
    SetKineticNumber(20)
    SetShutter(0,1)
    run()
    save(#0,name$ + "conv1_dark.sif")
    ExportTiff(#0, name$ + "conv1_dark.tif", 1, 1, 0, 0)
    CloseWindow(#0)
    CloseWindow(#1)

    SetShutter(1,1)
    run()
    save(#0,name$ + "conv1_bright.sif")
    ExportTiff(#0, name$ + "conv1_bright.tif", 1, 1, 0, 0)
    CloseWindow(#0)
    CloseWindow(#1)

    SetOutputAmp(0)
    SetShutter(1,1)
    for i = 40 to 300 step 10
        SetGain(i)
        exp=~GetSaturatingExposure()
        print(exp)
        SetExposureTime(exp)
        SetKineticNumber(20)
        SetShutter(0,1)
        run()
```

A. EM-CCD camera calibration

```
    save(#0, name$ + str$(i) + "_dark.sif")
    ExportTiff(#0, name$ + str$(i) + "_dark.tif", 1, 1, 0, 0)
    CloseWindow(#0)
    CloseWindow(#1)
    SetShutter(1,1)
    run()
    save(#0, name$ + str$(i) + "_bright.sif")
    ExportTiff(#0, name$ + str$(i) + "_bright.tif", 1, 1, 0, 0)
    CloseWindow(#0)
    CloseWindow(#1)
next

SetOutputAmp(1)
print("conv_end")
exp= ~GetSaturatingExposure()
print(exp)
SetExposureTime(exp)
SetKineticNumber(20)
SetShutter(0,1)
run()
save(#0, name$ + "conv2_dark.sif")
ExportTiff(#0, name$ + "conv2_dark.tif", 1, 1, 0, 0)
CloseWindow(#0)
CloseWindow(#1)

SetShutter(1,1)
run()
save(#0, name$ + "conv2_bright.sif")
ExportTiff(#0, name$ + "conv2_bright.tif", 1, 1, 0, 0)
CloseWindow(#0)
CloseWindow(#1)
```

A. EM-CCD camera calibration

$gain_{\text{software}}$	$1/(M \cdot M_{\text{pre}})$ [e/ADU]	N_r [e/px]	$N_{(M)}/(W \times H)$ [e/px]	exposure [ADU]	$N'_{(M)}/(W \times H)$ [s]	$1/F_n$ [e/(px s)]
conv1	1.3165	7.189	3008.66	0.2016	14923	0.981
50	0.1160	0.486	260.05	0.0289	8995	0.591
60	0.0984	0.406	225.46	0.0249	9054	0.595
70	0.0841	0.349	190.52	0.0212	8983	0.591
80	0.0729	0.305	165.24	0.0186	8907	0.586
90	0.0680	0.288	150.54	0.0161	9368	0.616
100	0.0611	0.262	128.47	0.0136	9427	0.620
110	0.0550	0.241	121.11	0.0129	9409	0.619
120	0.0510	0.228	113.71	0.0120	9498	0.624
130	0.0465	0.211	106.66	0.0112	9541	0.627
140	0.0433	0.201	96.95	0.0101	9564	0.629
150	0.0405	0.192	89.68	0.0093	9671	0.636
160	0.0380	0.183	87.24	0.0090	9656	0.635
170	0.0359	0.175	81.56	0.0084	9739	0.640
180	0.0339	0.169	79.80	0.0081	9863	0.648
190	0.0321	0.163	74.00	0.0075	9806	0.645
200	0.0305	0.158	72.57	0.0073	9878	0.649
210	0.0292	0.155	69.44	0.0070	9944	0.654
220	0.0280	0.150	67.69	0.0068	9971	0.656
230	0.0268	0.147	65.63	0.0065	10057	0.661
240	0.0257	0.188	63.90	0.0063	10131	0.666
250	0.0244	0.140	62.52	0.0062	10026	0.659
260	0.0237	0.137	62.86	0.0062	10078	0.663
270	0.0229	0.135	63.17	0.0062	10130	0.666
280	0.0221	0.133	63.64	0.0062	10204	0.671
290	0.0214	0.130	63.38	0.0062	10162	0.668
300	0.0205	0.128	63.20	0.0062	10133	0.666
conv2	1.5953	8.768	8198.86	0.5291	15496	1.019

Table A.1.: Comparison of read noise for different EM-gain settings (first column) of the Andor Ixon3. W and H are the size of the sensor (in pixels). The value $N'_{(M)}$ estimates the number of photoelectrons the detector would have seen with 1 s integration time and is used to calculate the excess noise factor in the last column. In EM-mode the fastest readout speed was used 10 MHz with vertical shift speed of 1.7 μ s.

{tab:ixon-table}

A. EM-CCD camera calibration

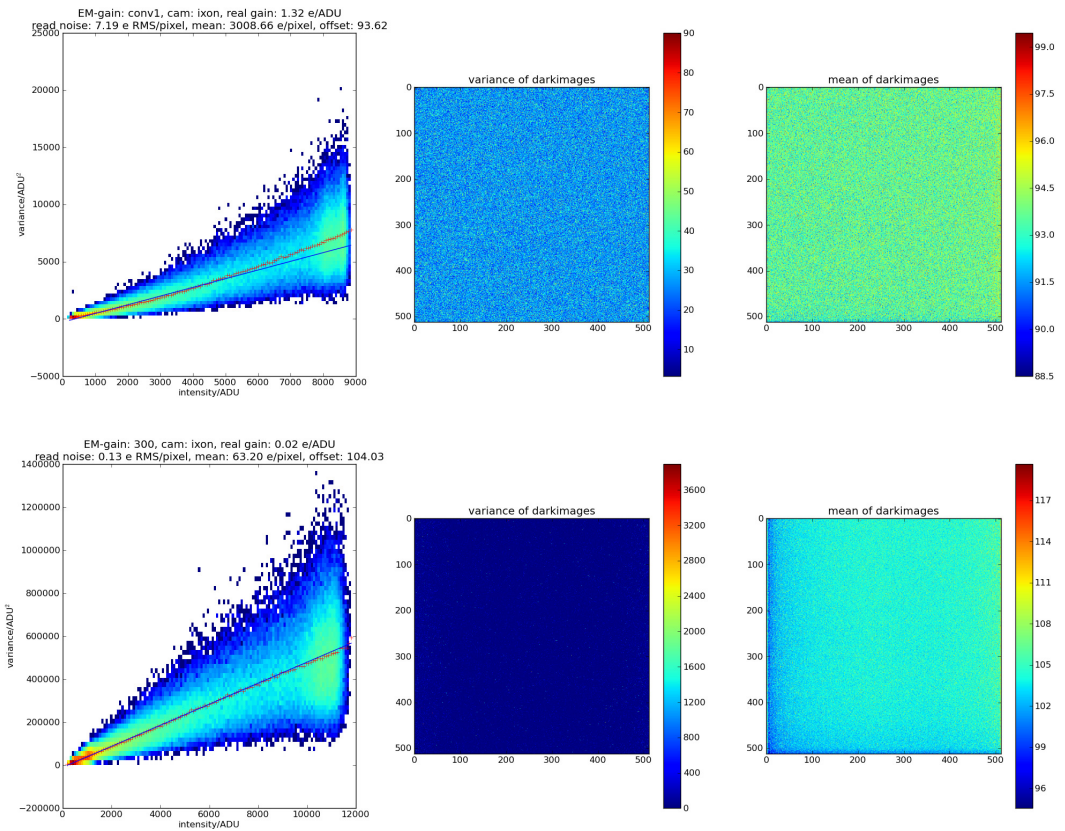


Figure A.1.: Readnoise evaluation using the Python code in section A.2 **top:** Conventional readout of an Andor Ixon3 camera. **bottom:** readout with an EM-gain setting of 300 on the same camera with identical sample. **left:** 2D histogram of per pixel variances against binned intensities. **middle:** variance of 20 dark images. **right:** mean of 20 dark images.

?(fig:ixon)?

A.2. Python code listing for the read noise evaluation

```
python-readnoise-eval>#!/usr/bin/env python
# ./ti.py /media/backup/andor-ultra-ixon/martin/20111111/scan-em3/ ultra 2700
import sys
import os

import matplotlib
matplotlib.use('Agg')

from pylab import *
from libtiff import TIFFfile, TIFFimage
from scipy import stats

seterr(divide='ignore')

folder = sys.argv[1]
cam = sys.argv[2]
gain = sys.argv[3]
```

A. EM-CCD camera calibration

```

def readpics(gain, cam='ixon_', isdark=False):
    print 'loading ', os.path.join(folder, cam) + '_' + gain + '_bright.tif'
    fg=TIFFfile(os.path.join(folder, cam) + '_' + gain + '_bright.tif')
    bright,bright_names=fg.get_samples()
    bg=TIFFfile(os.path.join(folder, cam) + '_' + gain + '_dark.tif')
    dark,dark_names=bg.get_samples()
    return (bright[0],dark[0])

(f,b) = readpics(gain=gain, cam=cam)

bg=mean(b, axis=0)
v=var(f, axis=0)
i=mean(f, axis=0)

ny,nx=64,128
H,y,x=histogram2d(v.flatten(),i.flatten(),bins=[ny,nx],
                    range=[[0,v.max()], [0,i.max()]])
extent = [x[0], x[-1], y[0], y[-1]]
acc=zeros(x.shape, dtype=float64)
accn=zeros(x.shape, dtype=int64)
s=nx/i.max()
for ii, vv in nditer([i,v]):
    p=round(ii*s)
    acc[p]+=vv
    accn[p]+=1

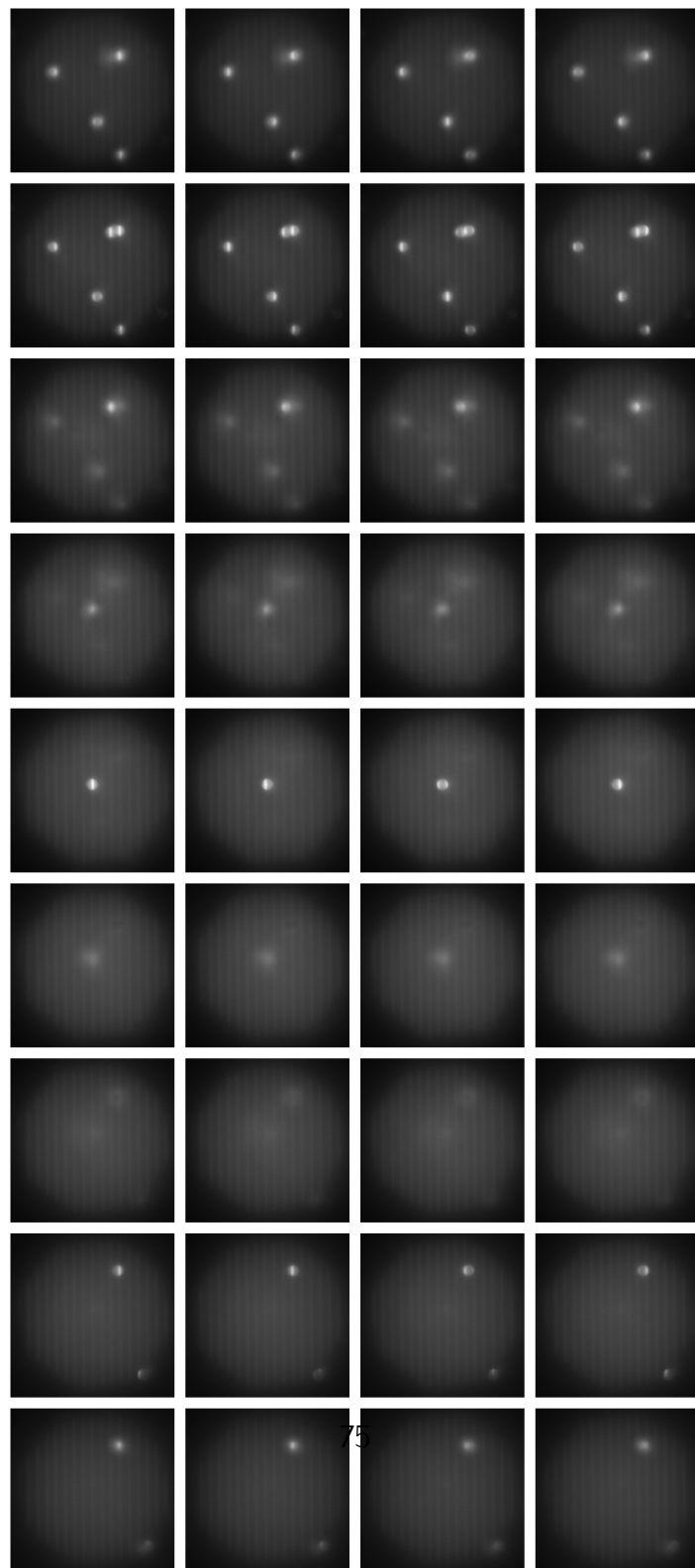
fig=figure(figsize=(24, 8), dpi=300)
hold(False)
title('bal')
subplot(1,3,1)
imshow(log(H), extent=extent,
       aspect='auto', interpolation='none', origin='lower')
hold(True)
ax=x[nonzero(accn)]
ay=acc/accn
ay=ay[nonzero(accn)]
l=round(.6*len(ax))
bx=ax[0:l]
by=ay[0:l]
plot(ax,ay,'r+')
slope,intercept,rval,pval,stderr=stats.linregress(bx,by)
plot(ax,polyval([slope,intercept],ax))
xlabel('intensity/ADU')
ylabel(r'variance/ADU$^2$')
real_gain=1/slope # unit electrons/ADU
read_noise=sqrt(var(b))*real_gain # electrons RMS per pixel
mean_elecs=(mean(f)-mean(b))*real_gain # photoelectrons electrons per pixel
print gain, cam, real_gain, read_noise, mean_elecs, mean(b), rval, pval, stderr
tit='EM-gain: %s, cam: %s, real gain: %.2f e/ADU\n'
read noise: %.2f e RMS/pixel, mean: %.2f e/pixel, offset: %.2f'
% (gain, cam, real_gain, read_noise, mean_elecs, mean(b))
title(tit)
subplot(1,3,2)
imshow(var(b, axis=0))
title('variance of darkimages')
colorbar()
subplot(1,3,3)

```

A. EM-CCD camera calibration

```
imshow(mean(b, axis=0))
title('mean of darkimages')
colorbar()
show()
fig.savefig(cam+'_'+gain+'.png')
```


B. Optical sectioning by structured illumination



Bibliography

- Abramoff** [1] M. D. Abràmoff, I. Hospitals, P. J. Magalhães, and M. Abràmoff. Image Processing with ImageJ. *Biophotonics International*, 2004.
- Adams2010** [2] A. Adams, M. Horowitz, S. H. Park, N. Gelfand, J. Baek, W. Matusik, M. Levoy, D. E. Jacobs, J. Dolson, M. Tico, K. Pulli, E.-V. Talvala, B. Ajdin, D. Vaquero, and H. P. a. Lensch. The Frankencamera. *ACM Transactions on Graphics*, 29(4):1, July 2010. ISSN 07300301. doi: 10.1145/1778765.1778766. URL <http://portal.acm.org/citation.cfm?doid=1778765.1778766>.
- Berndt2007** [3] D. Berndt. *Software fuer die zeitoptimierte Kalibrierung von Mikrokippsspiegeln*. PhD thesis, Dresden, 2007.
- Berndt2010** [4] D. Berndt, J. Heber, S. Sinning, D. Kunze, J. Knobbe, J.-U. Schmidt, M. Bring, D. Rudloff, M. Friedrichs, J. Roessler, M. Eckert, W. Kluge, H. Neumann, M. Wagner, and H. Lakner. Multispectral characterization of diffractive micromirror arrays. In *Proc. SPIE 7718*, volume 7718, 2010.
- Berndt2011** [5] D. Berndt, J. Heber, S. Sinning, and D. Rudloff. Calibration of diffractive micromirror arrays for microscopy applications. *Proc. SPIE 8191*, 81910O, 2011. doi: <http://dx.doi.org/10.1117/12.899881>.
- Branco2010** [6] T. Branco, B. a. Clark, and M. Häusser. Dendritic discrimination of temporal input sequences in cortical neurons. *Science (New York, N.Y.)*, 329(5999):1671–5, Sept. 2010. ISSN 1095-9203. doi: 10.1126/science.1189664. URL <http://www.ncbi.nlm.nih.gov/pubmed/20705816>.
- Caarls2011** [7] W. Caarls, B. Rieger, A. H. B. De Vries, D. J. Arndt-Jovin, and T. M. Jovin. Minimizing light exposure with the programmable array microscope. *Journal of microscopy*, 241(1):101–110, Jan. 2011. ISSN 1365-2818. doi: 10.1111/j.1365-2818.2010.03413.x. URL <http://www.ncbi.nlm.nih.gov/pubmed/21118211>.
- Denk1990** [8] W. Denk, J. H. Strickler, and W. W. Webb. Two-photon laser scanning fluorescence microscopy. *Science*, 245, 1990.

Bibliography

- Edelstein2010** [9] A. Edelstein, N. Amodaj, K. Hoover, R. Vale, and N. Stuurman. Computer Control of Microscopes Using μ Manager. In *Current Protocols in Molecular Biology*, number October, pages 14.20.1–14.20.17. John Wiley & Sons, Inc., 2010. ISBN 9780471142720. doi: 10.1002/0471142727.mb1420s92.
- Gustafsson1999** [10] M. G. L. Gustafsson, D. A. Agard, and J. W. Sedat. I5M: 3D widefield light microscopy with better than 100 nm axial resolution. *Journal of Microscopy*, 195(July):10–16, 1999.
- Heintzmann2010a** [11] R. Heintzmann and K. Wicker. Optical devices and Methods, 2010.
- Hope1999** [12] I. Hope. *C. elegans: a practical approach*. Oxford University Press, Oxford, 1999. URL http://books.google.com/books?hl=en&lr=&id=B5JJaHa3JlgC&oi=fnd&pg=PR17&dq=C.+elegans:+A+Practical+Approach&ots=_FyXstupGY&sig=QlIY3tSNFRugKG002T91Fp6ZsOY.
- Huisken2004** [13] J. Huisken, J. Swoger, F. Del Bene, J. Wittbrodt, and E. H. K. Stelzer. Optical Sectioning Deep Inside Live Embryos by Selective Plane Illumination Microscopy. *Science*, 305(5686):1007–1009, Aug. 2004. ISSN 0036-8075. doi: 10.1126/science.1100035. URL <http://www.lmg.embl.de/pdf/huisken04.pdf>.
- Ipp2009** [14] E. Ipp, J. Wenisch, and A. Jacobsen. Deliverable 8.04 Initial MMA/Optics evaluation system (refractive) v1.2. Technical report, In-Vision, 2009a.
- Ipp2009a** [15] E. Ipp, J. Wenisch, A. Jacobsen, and G. Zöchling. Deliverable 8.09 Final design of refractive optical systems. Technical report, In-Vision, 2009b.
- Koshel2012** [16] R. Koshel. *Illumination Engineering: Design with Nonimaging Optics*. Wiley, 2012. ISBN 9781118462492. URL http://books.google.com/books?hl=en&lr=&id=WpL2SQoJCXYC&oi=fnd&pg=PR2&dq=Illumination+Engineering:+Design+with+Nonimaging+Optics&ots=7gJQ4QgdFp&sig=sTUpKAHR-GEA_d5BpVuGoZgNdAc.
- levoy2006** [17] M. Levoy, R. Ng, A. Adams, M. Footer, and M. Horowitz. Light field microscopy. *ACM Trans. Graph.*, 25(3):924–934, July 2006. ISSN 0730-0301. doi: <http://doi.acm.org/10.1145/1141911.1141976>.
- tinez-Garcia2009** [18] A. Martínez-García, I. Moreno, M. M. Sánchez-López, and P. García-Martínez. Operational modes of a ferroelectric LCoS modulator for displaying binary polarization, amplitude, and phase diffraction gratings. *Applied optics*, 48(15):2903–14, May 2009. ISSN 1539-4522. URL <http://www.ncbi.nlm.nih.gov/pubmed/19458742>.

Bibliography

- [Matthae2003][19] W. Mattheae, Manfred and Schreiber, Lothar and Faulstich, Andreas and Kleinschmidt. High Aperture Objective Lens, 2003.
- [Mertz2010][20] J. Mertz and J. Kim. Scanning light-sheet microscopy in the whole mouse brain with HiLo background rejection. *Journal of biomedical optics*, 15(1):016027, 2010. ISSN 1560-2281. doi: 10.1117/1.3324890. URL <http://www.ncbi.nlm.nih.gov/pmc/articles/PMC2917465/>&tool=pmcentrez&rendertype=abstract.
- [Murray2006][21] J. I. Murray, Z. Bao, T. J. Boyle, and R. H. Waterston. The lineage of fluorescently-labeled *Caenorhabditis elegans* embryos with StarryNite and AceTree. *Nature protocols*, 1(3):1468–76, Jan. 2006. ISSN 1750-2799. doi: 10.1038/nprot.2006.222. URL <http://www.ncbi.nlm.nih.gov/pmc/articles/PMC1740643/>.
- [Rhodes2008][22] C. Rhodes. SBCL: A Sanely-Bootstrappable Common Lisp. In R. Hirschfeld and K. Rose, editors, *Self-Sustaining Systems*, pages 74–86. Springer Berlin / Heidelberg, 2008.
- [Ruckerl][23] F. Ruckerl, M. Kielhorn, J.-y. Tinevez, J. Heber, R. Heintzmann, S. Shorte, I. Pasteur, I. Dynamique, A.-e. Str, R. Division, and M. Biophysics. Micro mirror arrays as high-resolution , spatial light modulators for photoactivation and optogenetics. In *SPIE*, volume 33, 2013.
- [Santella2010][24] A. Santella, Z. Du, S. Nowotschin, A.-K. A. Hadjantonakis, and Z. Bao. A hybrid blob-slice model for accurate and efficient detection of fluorescence labeled nuclei in 3D. *BMC bioinformatics*, 11(1):580, 2010. ISSN 1471-2105. doi: 10.1186/1471-2105-11-580. URL <http://www.biomedcentral.com/1471-2105/11/580>.
- [Schindelin2012][25] J. Schindelin, I. Arganda-carreras, E. Frise, V. Kaynig, M. Longair, T. Pietzsch, S. Preibisch, C. Rueden, S. Saalfeld, B. Schmid, J.-y. Tinevez, D. J. White, V. Hartenstein, K. Eliceiri, P. Tomancak, and A. Cardona. Fiji: an open-source platform for biological-image analysis. *Nature Methods*, 9(7), 2012. doi: 10.1038/nmeth.2019.
- [Schmidt2010][26] J. U. Schmidt, M. Bring, J. Heber, M. Friedrichs, D. Rudloff, J. Rossler, D. Berndt, H. Neumann, W. Kluge, M. Eckert, M. List, M. Mueller, and M. Wagner. Technology development of diffractive micromirror arrays for the deep ultraviolet to the near-infrared spectral range. In H. Thienpont, P. V. Daele, J. Mohr, and H. Zappe, editors, *MICRO-OPTICS 2010*, volume 7716 of *Proceedings of SPIE-The International Society for Optical Engineering*, 2010. ISBN 978-0-8194-8189-4. doi: 10.1117/12.855750.